Preservation and characteristics of Organic Carbon in submarine lobe deposits of the Battfjellet Formation, Svalbard

Universiteit Utrecht | Faculty of Geosciences

MSc. Thesis

Rixt van der Woning (0761079)

Supervisors

Dr. J. T. Eggenhuisen

Dr. ir. F. Peterse

February 29, 2024

Abstract

Organic Carbon (OC) burial in marine sediments is the second biggest sink of atmospheric CO_2 on a geological timescale. Little quantitative research has been done on OC preservation in turbidite systems and OC preservation is poorly constrained, despite turbidites being reported as an important OC sink. This thesis investigates the extent to which turbidites are substantial OC sinks using quantitative data. This is achieved by analyzing the distribution of Particulate Organic Carbon (POC) size, Total Organic Carbon (TOC), and OC source ($\delta^{13}C$) of 66 samples from a sandy turbidite lobe of the Battfjellet Formation, deposited during the Eocene on Svalbard. Results are compared to pre-existing logs and mineral grain size distributions. Results show that POC size decreases in the lobe from 2.81 ϕ (Krumbein phi scale, 0.17 mm) in the most proximal sub-environment to 3.07 ϕ (0.14 mm) in the distal sub-environment due to hydrodynamic sorting. TOC values increase from an average 0.19wt% at the most proximal location to 0.38wt% at the most distal location, again as a result of hydrodynamic sorting. Stable carbon isotope analysis reveals that the proximal sub-environment has a largely terrestrial input with an average $\delta^{13}C$ value of -20.9‰, with an increasing marine input in the distal fringe sub-environment at an average $\delta^{13}C$ value of -23.7‰. Average TOC content is integrated over the volume of the lobe, the total amount preserved in the sandy lobe is at least 2001 kg OC/km^2/yr. What sets this turbidite lobe apart from other marine sediments is burial rate, where sedimentation rates in turbidite lobes are several magnitudes larger than in surrounding marine sediments, enabling lobes to much more OC. Mapping OC burial in turbidites is essential to better model a carbon cycle on a geological timescale as well as in current systems. This thesis serves as a first step towards this objective.

Keywords: *Turbidity currents*, *submarine lobe, Organic Carbon preservation, Battfjellet Formation, Eocene Carbon cycle*

Table of Contents

Introduction

Burial of organic carbon in marine sediments is the second biggest sink of atmospheric CO_2 on a geological scale, after silicate mineral weathering (Gaillardet et al., 1999). Turbidity currents are some of the most important sediment transport processes, with the ability to carry up to ten times more sediment in one flow than the world's yearly sediment input from rivers combined (Milliman and Syvitski, 1992; Talling et al., 2012). While research on carbon burial in marine sediments is extensive (Paradis et al., 2023), very little quantitative research on turbidite systems has been done (Hage et al., 2020). Quantifying the amount of atmospheric CO_2 that is stored in turbidite systems enables us to better model a carbon cycle that includes turbidites in the marine sediment sink. Applying a quantitative carbon budget estimation to turbidite systems from the Eocene allows us to better understand the Eocene carbon cycle (Fig. 1) and connect present and ancient OC burial and sequestration.

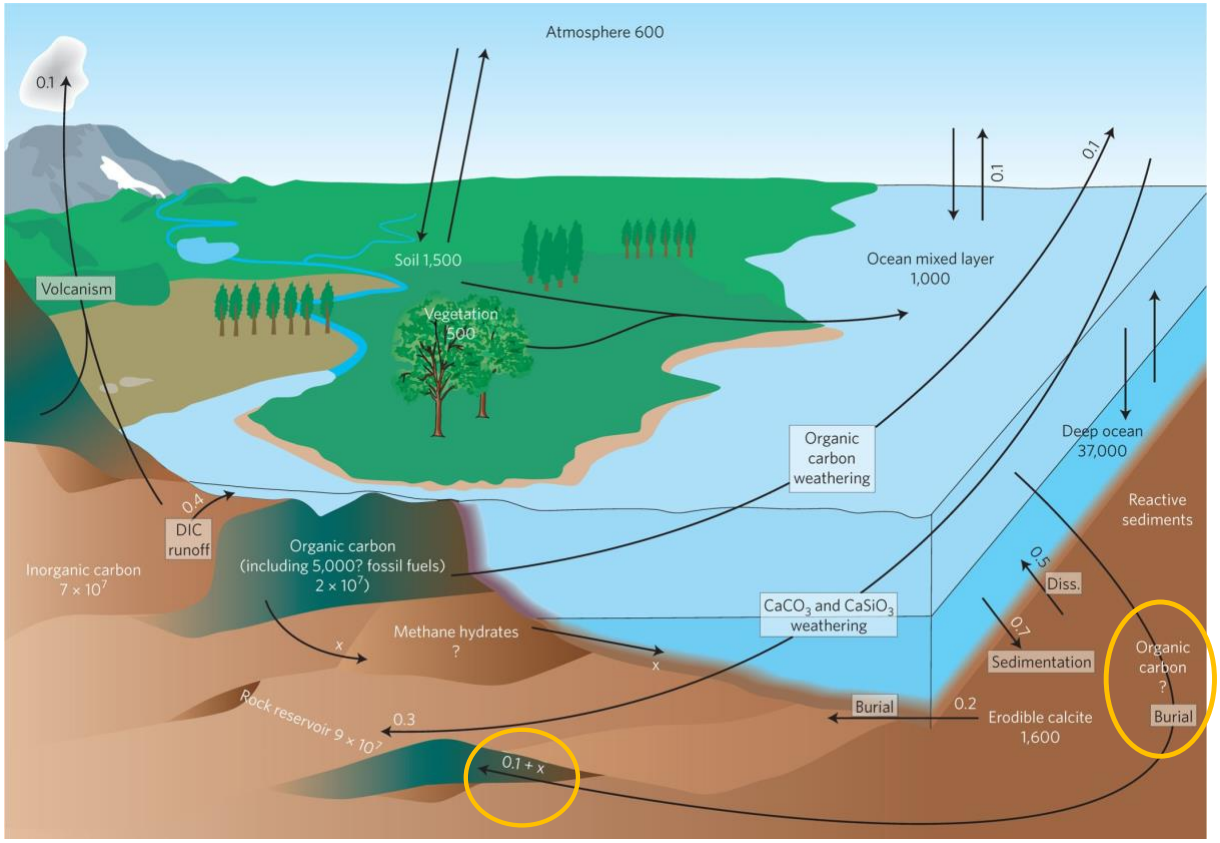

Figure 1: carbon reservoirs and fluxes during the Eocene, where fluxes shown are relevant to the timescale presented in the paper, and where the ocean-atmosphere-biosphere-system is assumed to be in equilibrium (Sluijs et al., 2013), reservoirs are in Pg and fluxes in Pg/yr. Carbon burial rates and preservation (highlighted with orange circles) are still largely unidentified.

Buried carbon in marine sediments usually has three sources, terrestrial, petrogenic and marine. No distinction can be made between petrogenic and terrestrial carbon due to the age of the samples, thus both are hereafter called terrestrial carbon. Stable carbon isotopes ($\delta^{13}C$) end members are inclined to change with pCO_2 values, resulting in differing $\delta^{13}C$ values during the Eocene compared to current end members (Sluijs and Dickens, 2012). Generally, terrestrial OC has a $\delta^{13}C$ value of at least -25‰ in modern systems (Kao et al., 2014; Masson et al., 2010; Sparkes et al., 2015), as opposed to the terrestrial endmember of around -23‰ during the Eocene (Sluijs and Dickens, 2012). Atmospheric CO_2 is stored in vegetation via photosynthesis, after which plant debris is carried to the ocean by rivers

(Galy et al., 2007). Terrestrial organic matter is refractory and often better preserved than marine organic matter (Hedges and Keil, 1995). Marine OC currently has $\delta^{13}C$ values between -17 and -22‰, (Kao et al., 2014; Masson et al., 2010; Sparkes et al., 2015), while the marine end member of OC was around -27‰ during the Eocene (Sluijs and Dickens, 2012). Furthermore, marine OC is more reactive and is often remineralized (Hedges and Keil, 1995). Marine OC consists of marine primary producers such as phytoplankton, also storing atmospheric CO_2 via photosynthesis (Bianchi and Bauer, 2011). While terrestrial carbon most likely predominates in our Eocene turbidite system from Svalbard based on previous research (Doerner et al., 2020; Grundvåg et al., 2023; Helland-Hansen, 2010), marine OC is often also present. There are numerous reasons for preferential burial of terrestrial OC in marine sediments, such as the depositional system dynamics of sedimentation rate and sediment exhumation (Stetten et al., 2015). In fine-grained sediments pore spaces are small and surface area is high, often with a high OC content, that shields OC from degradation (Mayer, 1994). Previous research indicates that the accumulation of fine-grained sediment seems to be the key of OC preservation (Hedges and Keil, 1995; Kennedy and Wagner, 2011), however OC preservation in coarser sand has long been disregarded (Sparkes et al., 2015). Sandy turbidites were initially assessed to be OC-free (Burdige, 2007), but recent studies show that organic matter can be found everywhere throughout the sandy deposits (Lee et al., 2019; McArthur et al., 2016; Saller et al., 2006). Sandy turbidites have been completely disregarded in existing carbon fluxes, thus this research intends to give a quantitative overview of OC preservation in sandy turbidites to improve global carbon fluxes (Burdige, 2007).

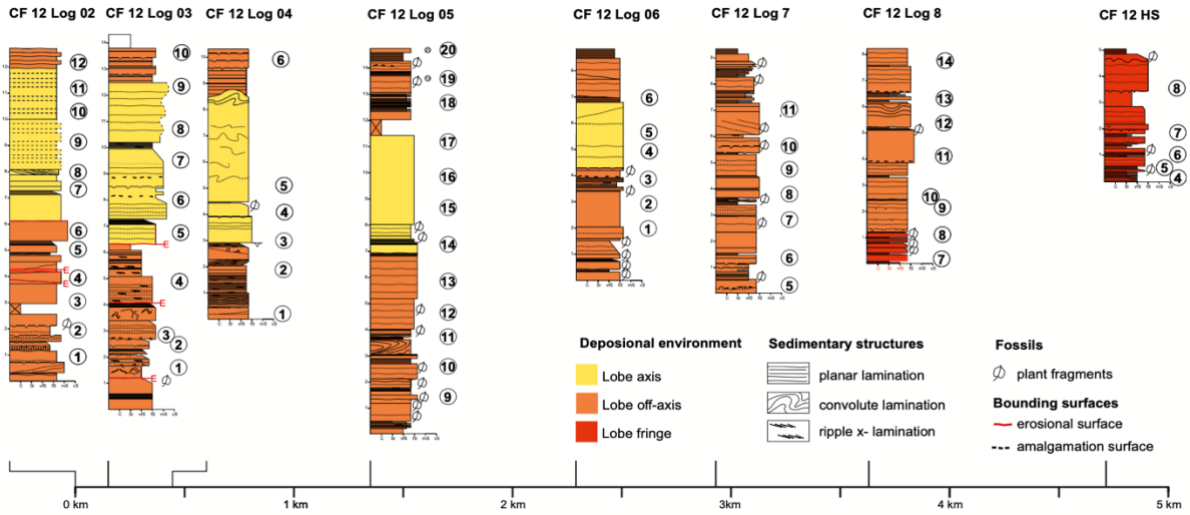

Figure 2: Sample locations with sample numbers per log, taken within deposits of the youngest lobe of Clinothem 12. Colours indicate the interpreted lobe sub-environment based on field data (Spychala et al., 2021).

This study investigates how turbidity currents function as a carbon sink and how much organic carbon (OC) is preserved in sandy turbidites on geological timescales using TOC analysis. Previously published literature (Galy et al., 2007; Hage et al., 2020; Kao et al., 2014; Masson et al., 2010; Stetten et al., 2015) shows that OC buried in turbidites has a significant terrestrial origin. Stable carbon isotope analyses will confirm whether this is also the case for the turbidites of the Eocene Battfjellet Formation from Svalbard, based on differing marine and terrestrial $\delta^{13}C$ end members. Furthermore, this research will contribute to our understanding of Total Organic Carbon (TOC) preservation and distribution in turbidites.

The quartz-dominated sandstones found in the basin-floor deposits of Clinothem 12 of the Battfjellet Formation (Central Tertiary Basin (Svalbard)) (Steel and Olsen, 2002) pose as an excellent research area. The turbidites of the Battfjellet Formation largely consist of shelf to slope deposits, of which parasequences locally extend into the basin and reach basin-floor fan-systems (Helland-Hansen, 1990). One such clinothem reaching the basin-floor is well preserved in Clinothem 12, located around the Storvola and Hyrnestabben area. Clinothem 12 gives a complete overview of a lobe complex with good proximal to distal preservation (Spychala et al., 2021). The lobe complex consists of two lobes, of which the youngest is the focus of this thesis (Fig. 2).

The fact that the Battfjellet Formation has been thoroughly studied (Grundvåg et al., 2023) allows for the data to be put in a larger geological framework. The data is compared to mineral sand grain size distributions and to a depositional sub-environment and facies model of the lobe (Fig. 2), as presented by Spychala et al. (2021). Each sample presented in the correlation panel (Fig. 2) is also used in this thesis. The depositional model consists of the axis, off-axis, fringe, and distal fringe sub-environments (Fig. 3), which are interpreted based on lithofacies associations presented in their paper and correspond to the distinct hierarchical level of a lobe (Prélat et al., 2009).

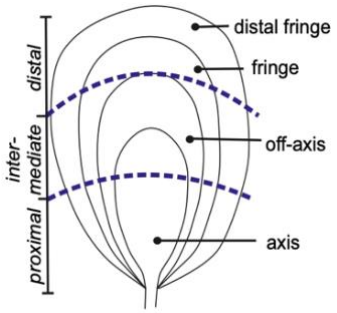

Figure 3: schematic overview of the different sub-environments of a lobe from Spychala et al. (2021).

This thesis contains a chemical and a thin section analysis. Chemical analyses look at the characteristics of the Organic Carbon. Total Organic Carbon (TOC) analysis looks at the organic carbon content in crushed samples and stable carbon isotope analysis determines the source of the carbon. Thin section analysis is used to determine the size of the carbon particles. The specific objectives of the thesis are to a) determine the Total Organic Carbon content of each sample and map the TOC distribution of the youngest lobe of the lobe complex of Clinothem 12 to determine the OC sequestering potential in turbidite lobes, b) determine whether the source of the Organic Carbon in Clinothem 12 is terrestrial or marine with stable carbon isotopes ($\delta^{13}C$), and c) study the particle size distribution of Particulate Organic Carbon in the lobe to analyze the physical behaviour of POC in turbidite systems and compare POC size distribution with mineral grain size distribution to see if there is parity or disparity in trends. This research will give a quantitative estimate of how much Organic Carbon is preserved in an Eocene turbidite lobe of the Battfjellet Formation. Ultimately, this research this thesis serves as a first step towards quantitively mapping OC burial in turbidite lobes to better model a carbon cycle.

Geological setting

Formation of the Central Basin

The Central Basin or Central Tertiary Basin is located in southwest Spitsbergen (Fig. 4). The Central Basin and the adjacent West-Spitsbergen Fold and Thrust Belt (WSFTB) formed during a dextral strike-slip phase in the Early Paleocene, as the North Atlantic and the Arctic seaways opened (Helland-Hansen, 2010; Helland-Hansen and Grundvåg, 2021; Müller and Spielhagen, 1990; Myhre et al., 1982; Steel et al., 1985). The opening of the north Atlantic was accommodated by transtension between the Eurasian and Greenland plates (Bergh et al., 1997; Helland-Hansen and Grundvåg, 2021) as a result of rifting and subsequent seafloor spreading in the Norwegian-Greenland Sea (Müller and Spielhagen, 1990). The fault system migrated towards the northeast during the Early Eocene, opening up the Greenland Sea (Myhre et al., 1982). The northward movement of Greenland during the Late Paleocene caused consequent transpression along the transform fault system (Müller and Spielhagen, 1990; Myhre et al., 1982), resulting in 20 – 40 km of shortening in west Svalbard, forming the West-Svalbard Fold and Thrust Belt and the foreland basin to its east (Braathen and Bergh, 1995; Helland-Hansen, 1990).

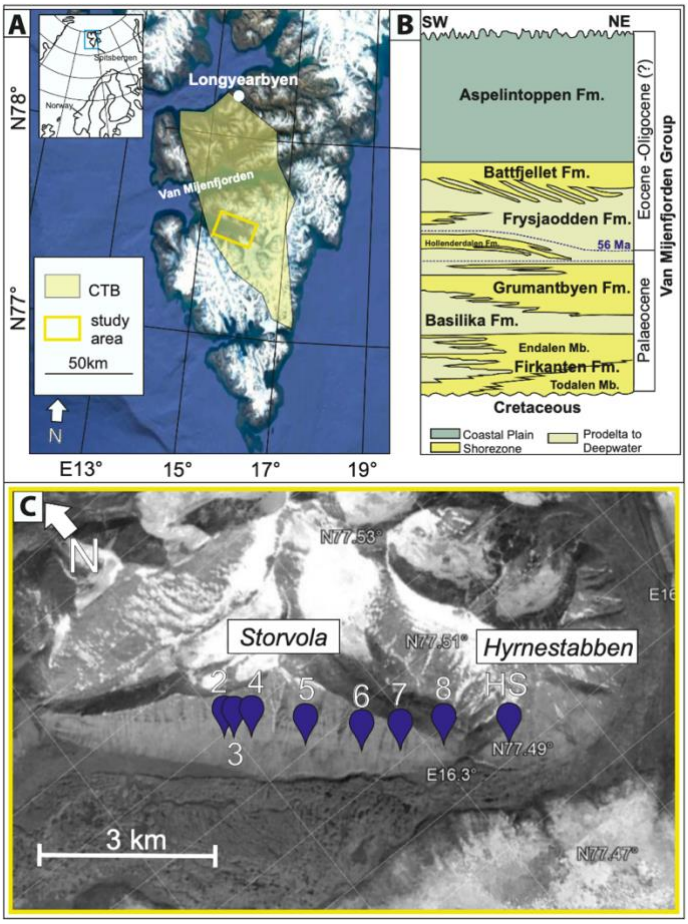

Figure 4: (A) Location of Central Tertiary Basin with the study area indicated with a rectangle. (B) Stratigraphy of the CTB (Crabaugh and Steel, 2004). (C) Locations of the outcrops in the Storvola and Hyrnestabben areas. From Spychala et al. (2021).

Paleogene on Svalbard

Deposits

The Central Basin is approximately 200 km long and 60 km wide and consists of the clastic Van Meijerfjorden Group (Fig. 4b) (Harland and Kay, 1969; Steel et al., 1985). The clastic material of the Van Meijerfjorden Group asymmetrically fills in the basin. Paleocene sediments are fed from sediment sources the east of the basin, depositing the Firkanten, Basilika and Grumantbyen Formations, after which drainage reversal takes place around the Paleocene-Eocene transition (Petersen et al., 2016). The Eocene and Oligocene material is transported by rivers from the west, draining the eastward migrating West-Spitsbergen Fold and Thrust Belt and depositing the subsequent sediments, now known as the Hollendardalen, Grumantbyen Frysjaodden, Battfjellet and Aspelintoppen Formations (Grundvåg et al., 2014b; Lasabuda et al., 2018; Petersen et al., 2016; Plink-Björklund et al., 2001; Steel et al., 1985). The Paleocene to Eocene deposits prograded eastward to southeastward, filling in the basin with coastal plain to basin-floor deposits (Helland-Hansen, 1990). Sedimentation occurred on

the basin-floor despite relative sea-level rise, indicating that sediment supply was high (Grundvåg et al., 2014b). High sediment supply caused shelf-edge and slope progradation, forcing the eastward to southeastward migration of the depocenter (Grundvåg et al., 2014b; Helland-Hansen, 1990). This resulted in a asymmetric sedimentary succession with a thickness of at least 1.5 km in the west to less than 600m in the east (Plink-Björklund et al., 2001), though thickness estimations differ: at least 800-1000m in the west to 300m in the east (e.g. (Helland-Hansen and Grundvåg, 2021; Steel et al., 1985).

Climate

Time constraints on the Central Basin are limited. Radiometric dating on bentonites at the base of the Frysjaodden Formation (Fig. 4) show an age of 56Ma (Charles, 2011). Due to the thickness of the deposits and determined fossil age (Manum and Throndsen, 1986) the age of the overlying Battfjellet Formation is assumed to be Eocene to Oligocene. Svalbard's paleolatitude during the Eocene-Oligocene is estimated at roughly 70-75°N based on paleomagnetic data (van Hinsbergen et al., 2015) and plant remains found in the Aspelintoppen Formation (Clifton, 2012). These plant remains belong to forests that grew only ~1500km away from the North Pole during the Eocene and Oligocene (Clifton, 2012). The plant remains compare to conifers that we see nowadays at similar latitudes (Schweitzer, 1980) and indicate a warm temperate climate with high precipitation rates (Clifton, 2012). Based on $\delta^{18}O$ values from benthic foraminifera, temperatures peaked with the Paleocene-Eocene Climatic Maximum (PETM) and the Early Eocene Climatic Optimum (EECO), which was followed by significant cooling during the Eocene and Oligocene (Fig. 5, Zachos et al., 2008).

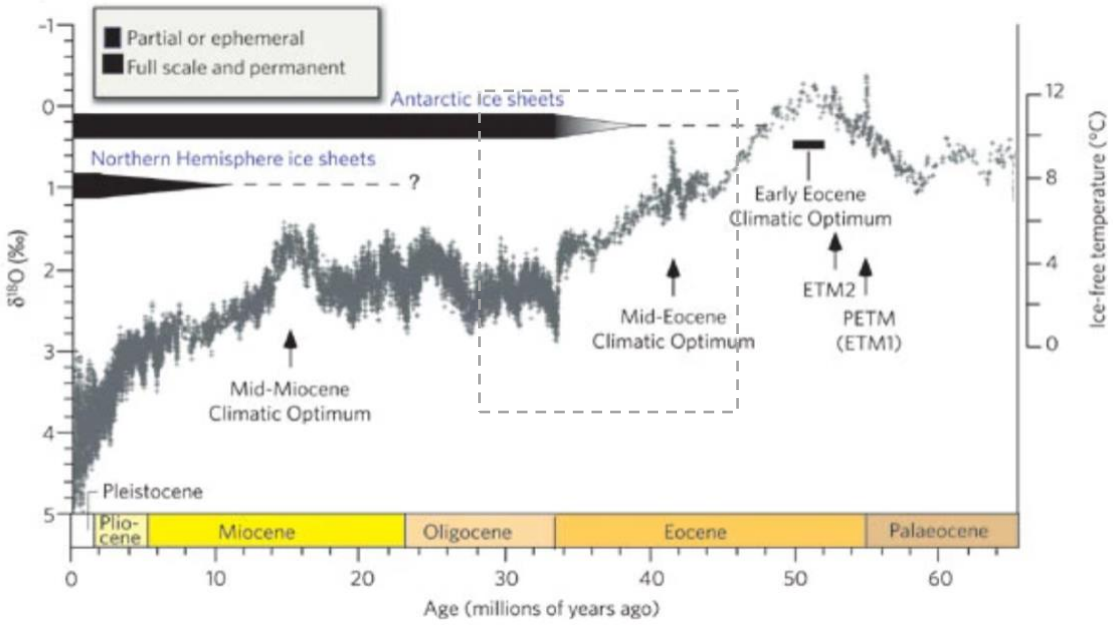

Figure 5: Cenozoic climate curve based on stacked benthic foraminiferal oxygen isotope records of Deep Sea Drilling Project and Ocean Drilling Program (Zachos et al., 2008), estimated age of the Battfjellet Formation indicated with dashed box.

Roots, tree trunks and leaves are abundant in the Firkanten (Todalen Member) and Aspelintoppen Formations, leading to high OC content and even coal seams in the Todalen Member. The Firkanten (Endalen Member), Grumantbyen and Battfjellet Formations consist of sandstones that harbor fossil horizons containing pelecypods, gastropods and occasionally arthropods (Dallmann, 2015). However, evidence for near-freezing temperatures during the Paleogene has been found. For example, sea ice transported pebbles of chert and granitic rocks formed elsewhere to the CTB where it was deposited

in the Eocene (Kellogg, 1975). Several paleofloristic studies agree that near freezing temperatures were reached (Golovneva, 2010; Uhl et al., 2007). Moreover, erratics and glendonites were found throughout the entire Paleogene (Spielhagen and Tripati, 2009), of which the latter is an indicator for OC-rich environments. Glendonites form in cold water (0-7^{o}C) as a pseudomorph from ikaite, which forms as a post-depositional mineral with marine organic matter as its main carbon source (Spielhagen and Tripati, 2009). Important to note is that erratics and glendonites were not found in the strata that contain warm climate indicators such as the plants and pelcypods or gastropods (Spielhagen and Tripati, 2009). In conclusion, the climate on Svalbard transitioned from greenhouse conditions to icehouse conditions during the Paleogene (Dallmann, 2015; Zachos et al., 2008). Climate proxies indicate a temperate climate with cold excursions, possibly indicating temporal or seasonal variability (Helland-Hansen and Grundvåg, 2021).

Battfjellet Formation

The Battfjellet Formation comprises several eastward dipping clinoforms that migrated towards the basin with amplitudes of 150 – 350m (Helland-Hansen, 1990; 1992; Helland-Hansen and Grundvåg, 2021; Plink-Björklund et al., 2001; Steel et al., 1985; Steel and Olsen, 2002). Individual clinoforms are exposed as up to 15km long complexes (Plink-Björklund and Steel, 2004), with a maximum 5km slope length and 3-4^{o} slope gradient (Johannessen and Steel, 2005; Steel and Olsen, 2002). There is a strong distinction between three series of progradational or aggradational clinoform sets, caused by third order growth cycles (1-2 Myr), likely due to tectonic control (Johannessen and Steel, 2005). Clinoforms 1 – 4 (Fig. 6) are progradationally stacked and represent the first clinoform set. The second set includes Clinothem 12, consists of clinoforms 5 – 14, and is aggradationally-then-progradationally stacked. The last set consists of the aggradationally-stacked clinoforms 15 – 20. Clinoforms 11 – 14 reach the basin-floor in a flat progradational shelf-edge trajectory, during aggradation of clinoforms 5 – 7 the sediments are stored on the shelf (Johannessen and Steel, 2005). Clinoforms 8 – 10 are suggested to reach the basin-floor, but cannot be proven due to outcrop limitations (Johannessen and Steel, 2005). Within the third order cycles, twenty clinoforms show regressive-then-transgressive cycles (Fig. 6; Johannessen and Steel, 2005; Steel and Olsen, 2002). The 20 clinoforms are deposited over fourth order cycles of some 100 Kyr (Johannessen and Steel, 2005; Steel and Olsen, 2002). The fourth order cycles are influenced by climate and are sensitive to eustatic sea-level changes (Johannessen and Steel, 2005).

The Battfjellet Formation serves as the transition between the time-equivalent marine offshore Frysjaodden Formation and the continental Aspelintoppen Formation, altogether forming an eastward prograding, regressive megasequence (Fig. 6) (Grundvåg et al., 2014a; Helland-Hansen, 2010; Plink-Björklund et al., 2006; Plink-Björklund and Steel, 2004; Steel and Olsen, 2002). The Battfjellet Formation consists largely of progradationally-stacked shelf to slope clinoform deposits (Grundvåg et al., 2014a; Helland-Hansen, 1990; Steel and Olsen, 2002), the topsets of the clinoforms are shelf or shallow marine deposits belonging to the Aspelintoppen Formation (Fig. 6). In some cases, the shoreline retreated immediately after clinoforms reached the shelf-slope break (Steel and Olsen, 2002). Sandy sediments were confined to basinward thinning wedges on the upper slope or even on the shelf as stacked deltaic or shoreface parasequences, characterized by coarsening upwards trends (Grundvåg et al., 2014a; Johannessen and Steel, 2005). In the events where the shoreline dropped below the shelf-slope break, large amounts of sand extended onto the clinoform slope (type 2) or in some cases even the basin-floor as a clinoform bottomset (type 1), both types creating sandy turbidite

fans (Crabaugh and Steel, 2004; Plink-Björklund and Steel, 2004; Steel and Olsen, 2002). Clinothem 12, the rock unit formed along clinoform 12 and the focus of this research, belongs to the latter.

The turbidites within Battfjellet Formation likely are fed by hyperpycnal flows along the margin of the Central Tertiary Basin (Helland-Hansen and Grundvåg, 2021; Petter and Steel, 2006; Plink-Björklund and Steel, 2004). Hyperpycnal flows generally carry very high suspended loads (Kneller and Buckee, 2000). Moreover, the type 1 deposits' progradational nature, coupled with bed amalgamation, indicates substantial sediment supply both on and from the shelf (Helland-Hansen and Grundvåg, 2021). The deposits demonstrate an immature character abundant in organic carbon, suggesting rapid deposition from the shelf-edge, with minimal reworking on both the slope and on the shelf, facilitated by the connection between the fluvial and turbidite channels (Helland-Hansen and Grundvåg, 2021; Plink-Björklund and Steel, 2004). The hyperpycnal flows are in the case of clinoform 12 fed beyond the shelf-edge during falling stage and lowstand system tracts (Plink-Björklund and Steel, 2004).

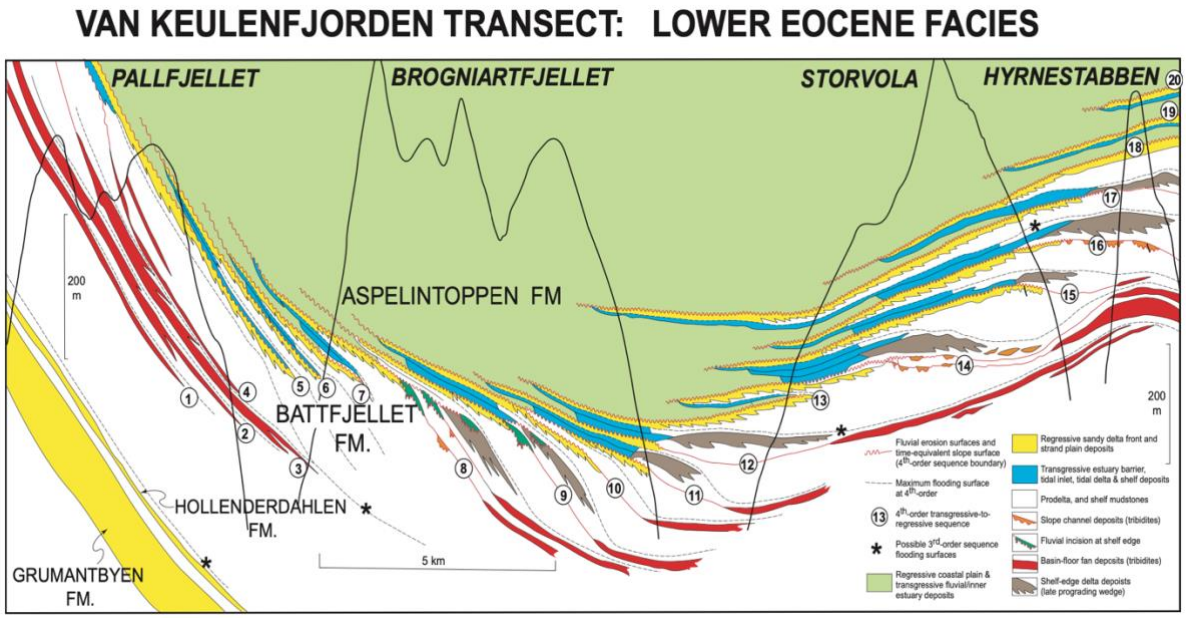

Figure 6: Sequence stratigraphic overview of the Lower Eocene in the Central Tertiary Basin, with 20 clinoforms linking the coastal plain deposits with the slope and basin-floor deposits. Some clinoforms (including Clinothem 12) extend onto the basin-floor. From Steel and Olsen (2002).

The slope to basin-floor deposits of the Battfjellet Formation are well preserved in Clinothem 12, located on the southwest flank of Storvola and Hyrnestabben (Fig. 4c). Its corresponding delta deposits occur west of the area (Steel and Olsen, 2002). The lobe complex discussed in this thesis belongs to Clinothem 12 and is approximately 10km long with a maximum thickness of 33m and pinches out near Hyrnestabben, where it is only 13m thick (Crabaugh and Steel, 2004; Spychala et al., 2021). The sandy deposits are characterized by two 15m-thick, sand-prone lobes consisting of fine sandy to maximum coarse sandy turbidites, separated by a 4.5m-thick heterolithic, silt-prone interlobe package (Crabaugh and Steel, 2004; Spychala et al., 2021). Clinothem 12 gives a complete overview of a lobe complex with good proximal to distal preservation, and a transition from high-density turbidity current deposits to low-density current deposits has been recognized in the lobe sub-environments (Spychala et al., 2021).

Methods

Sample selection

Samples of the turbidite deposit were collected during the 2017 fieldwork of Yvonne Spychala, Florian Pohl, Joris Eggenhuisen and Sten-Andreas Grundvåg. This research uses the same 66 samples from clinothem 12 that were used by Spychala et al. (2021). All 66 samples are located within the same lobe with a complete proximal to distal preservation, have complete logs and an overview of grain size analyses published by Spychala et al. (2021) (Fig. 2). Sandstone samples were collected every 1–2 m at the base of the sampled beds to avoid biasing towards specific bed divisions or sedimentary structures. Two means of evaluations are used to quantify the OC content and map its distribution within the turbidite lobes: a thin section and a chemical analysis. One thin section (CF12-HS-06) from the lobe fringe has disappeared since the paper was published and was therefore not used in the thin section analysis. One of the sandstone samples (CF12-8-13) from the lobe off-axis was too small to use for the chemical analysis, thus 65 samples were used.

Thin section analysis

Each thin section has a thickness of 30 µm and is photographed in high resolution under a petrographic microscope. The samples were analyzed automatically in image processing software ImageJ. The particle sizes of all OC particles in the thin sections were analyzed to create a large enough data set. There is a strong distinction in visibility on thin sections between Particulate Organic Carbon (POC) and OC that is matrix material, as matrix material is too fine-grained compared to particles. The OC in the matrix cannot be distinguished in this workflow and is thus disregarded in the thin section analysis. ImageJ fits an ellipse to the OC particle, taking into consideration the circularity, particle size and hole inclusion (Ferreira and Rasband, 2012), and registers the short and long axis. This ellipse has the same area, orientation, and centroid as the selected particle. Automatized image analysis requires size and colour threshold cut off values, of which the colour threshold value differs per scan due to lighting differences and requires human understanding.

The colour threshold is based on the blackness of the particles, as OC particles are opaque and show up completely black on thin sections (Fig. 7). ImageJ converts colour images to 8-bit images, resulting in the use of a greyscale threshold value where the complete opacity of OC particles is preserved as black particles. To better estimate which particles are OC, thin sections were evaluated using a petrographic microscope. As this analysis only looks at thin sections and not at chemical composition of selected particles, no distinction can be made between black opaque minerals and OC. This means that black opaque mineral grain sizes are also represented in the OC particle size distributions.

Measured grains that have a smaller diameter than the thin section thickness are difficult to identify and have a higher uncertainty due to possible overlapping grains (de Leeuw, 2017). Therefore, the size cut off value is based on the thickness of the thin section (30 µm). Different surface area cut off values were tested to find differences in the particle size distribution. A sample from the lobe axis (CF12-02-08) is used for this analysis and is presented in Figure 8. The smallest cut off value of 700µm^2 ultimately is used for processing. 700µm^2 is the area of the circle that corresponds to the minimal diameter of a grain that aligns with the human interpretation of POC, as particles smaller than this can be interpreted as matrix. Particles are still visible and interpreted as Particulate Organic Carbon at the

size of 700 µm^2 (Fig. 7). Using the smallest cut off value possible allows for a more inclusive overview of the particle size distribution.

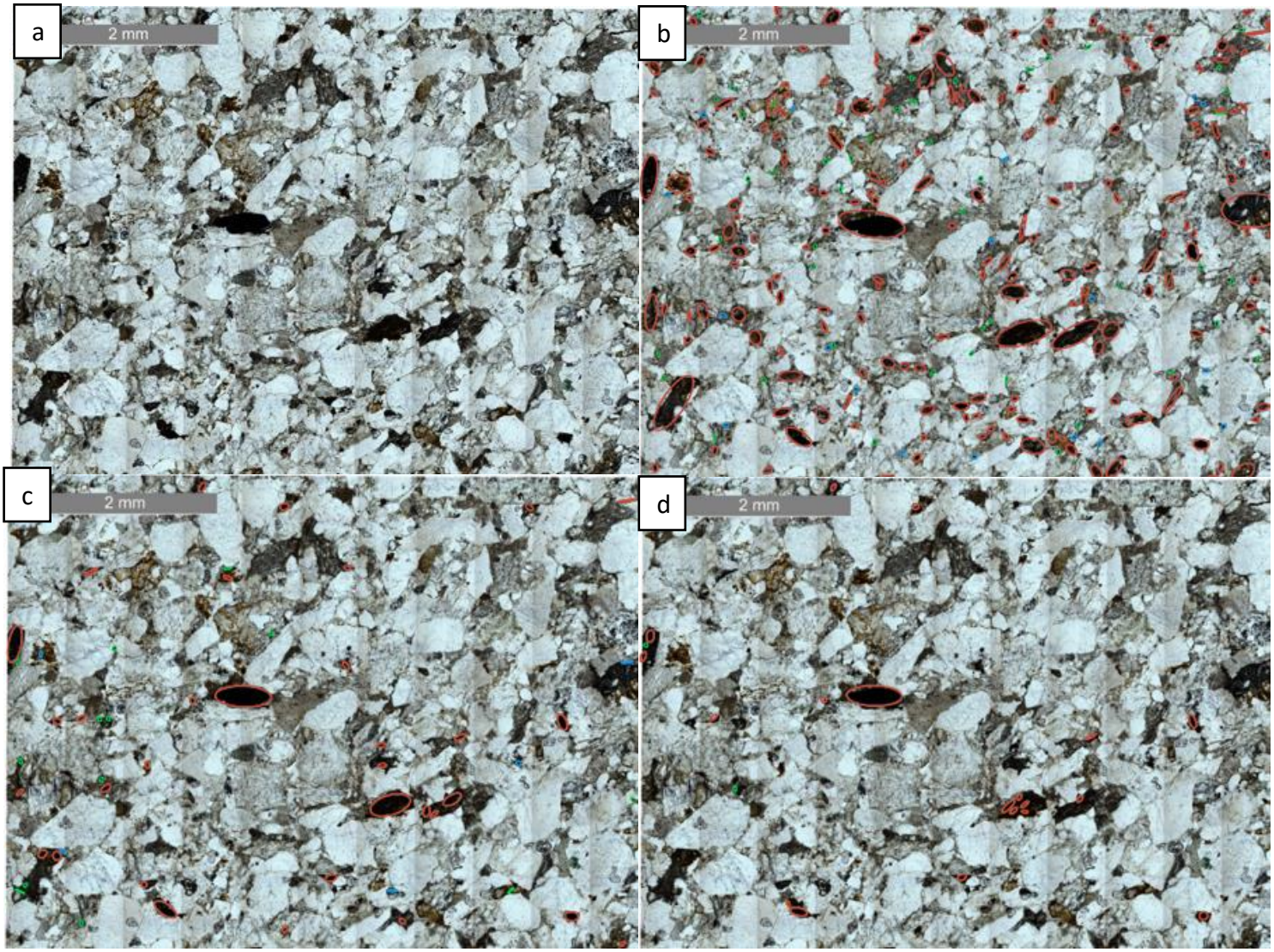

Figure 7: comparison between different grey value thresholds and cut-off values in thin-section CF12-02-08, with circles indicating the particles used for data analysis. Red circles indicate a size cut-off value of 1100µm^2, blue circles indicate 900 µm^2, green 700 µm^2. a) thin section with no annotations, b) thin section with a very high grey value threshold, c) thin section with the grey value threshold (darkest ~2%) used for analysis, d) thin section with a very low grey value threshold.

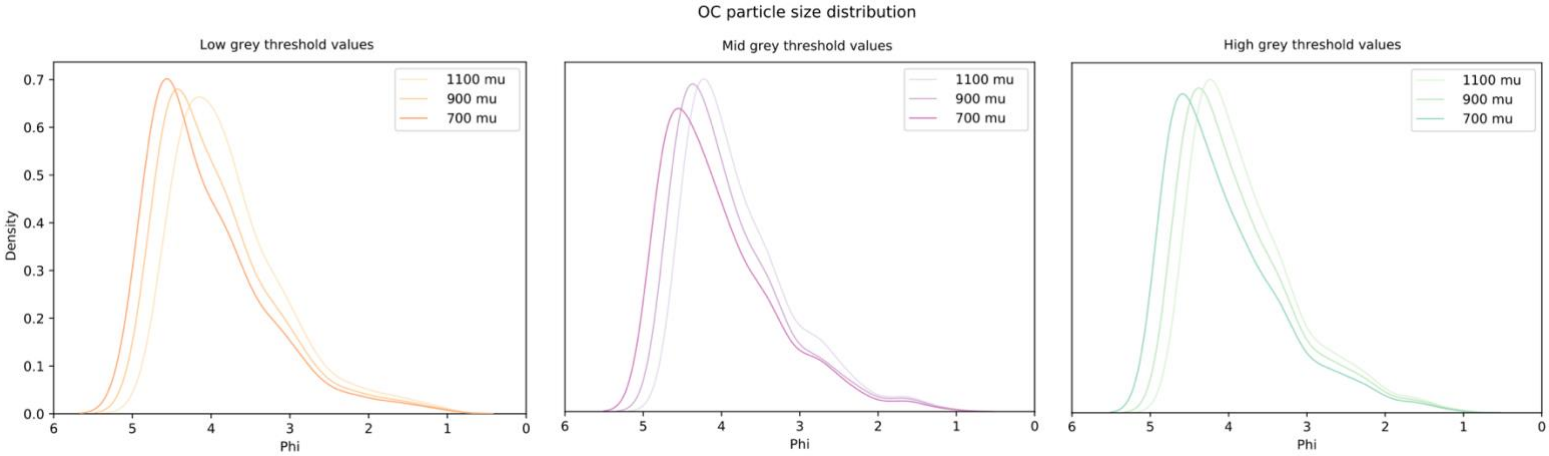

Figure 8: For each greyscale threshold, three size cut off values are considered. 700µm for inner circle corresponding to minimal diameter, 900µm for outer circle corresponding to a square (30x30µm), 1100µm for comparison how distribution shifts.

The automatically registered long (a) and short (b) axis are then used to determine the normal sectional diameter (*d'$_{mm}$),* which is in turn used to determine the true nominal diameter (*D'$_{mm}$*) of the particle. The axes are converted to millimeters and are corrected from observed to true axes (*a'* and *b'*), to account for underestimation of the ellipsoid particle (Johnson, 1994):

$$a'_{mm} = a_{\mu m} \cdot 1.1318 \cdot 0.001$$
$$d'_{mm} = (a'_{mm} \cdot b'_{mm})^{1/2}$$
$$D'_{mm} = d'_{mm} + 0.4(a'_{mm} - d'_{mm})^2$$

The true nominal diameters are then converted to the ϕ-scale (Krumbein, 1934) for the most widely accepted grain size data presentation (Johnson, 1994):

$$\varphi = -log_2(D_{mm})$$

All thin sections are plotted in one figure to compare particle size distributions. A kernel density estimation (KDE) is used for this, as this allows for a better analysis than a probability density function (PDF) in the case of differing sample group sizes. The KDE offers a smoother estimate of the PDF. A KDE takes into account the locations of all sample points and provides a convincing indication of multimodality (Węglarczyk, 2018). Box plots using all data were plotted to better visualize differences between depositional sub-environments.

Usually, grid point counting is used to determine grain size distributions in thin sections (Johnson, 1994). This method is suitable when grains align with grid points, however, due to the scarcity OC particles, all OC particles should be considered to create a large enough dataset. To include the probability factor that grid point counting entails, a specific weight is added to each measured size of a particle. The volume (*V*) of the particle determines the weight of each particle, as the volume dictates probability in a bulk sediment sample and bulk sediment is the most appropriate representation of grain size analyses (Kellerhals et al., 1975). The weighted mean ($\overline{D'_{mm}}$, or $\bar{\varphi}$)is calculated in Python, using the volume of the particle as its weight:

$$V = \frac{4}{3}\pi(\frac{1}{2} \cdot (0.001 \cdot D'_{mm}))^3$$
$$\overline{D'_{mm}} = \frac{\sum V \cdot D'_{mm}}{\sum V}$$

The weighted mean particle size of each thin section was plotted over distance to visualize how particle size changes over distance and per sub-environment. The complete size distribution is unknown due to a size cut off, causing visibly skewed density estimation. Hence, skewness and kurtosis are not looked at. Lastly, an ANOVA is applied to the weighted means of all thin sections to determine if the sub-environments are statistically different.

Bulk organic carbon properties

These analyses follow the same methodology as Kao et al. (2014) and Sparkes et al. (2015). Chemical analyses of TOC content and stable carbon isotopic composition include both particulate OC as well as OC in the matrix. All rocks were into small samples and any previously exposed surfaces are discarded to ensure samples are not contaminated with external OC. The small samples were then crushed into a fine, homogeneous powder with a Herzog crushing machine or manually with an agate

mortar. Between every sample, tools were thoroughly cleaned to prevent contamination. To ensure all measured carbon is of organic origin, all carbonate is removed, assuming all inorganic carbon is carbonate. Multiple decalcification techniques were tested to determine the most suitable method to remove inorganic carbon. The same crushed rock samples were used for the different decalcification techniques. Data testing showed that by using a second decalcification method without decantation, TOC values were higher and thus more OC was preserved, leading us to believe OC was indeed decanted and removed in the first method. For this reason, a second method is used for this thesis.

First decalcification method

The tube and cap of the samples were weighed. 25 ml HCl 1M is added to each sample at 20°C, after which the samples are shaken thoroughly in a machine for 4 hours. All samples are centrifuged for 10 minutes to separate the sediment from the liquid, the liquid is then decanted. This process is repeated to ensure samples are completely decalcified, the second time the shaking machine runs overnight. After treating the samples with acid twice, the acid is replaced by deionized water. The samples are shaken for 4 hours, centrifuged for 10 minutes, and decanted again. The deionized water process is repeated three times. The samples are moved to the oven to dry for 72 hours at 60 degrees, weighed again (with cap) and moved to the Elemental Analyzer.

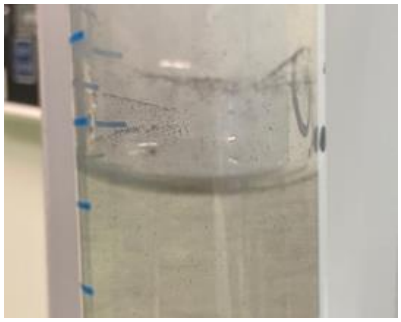

Figure 9: Black residue floating on top of one of the centrifuged samples.

The main problem with this first method is that black particles floated on top of the liquid during decalcification, even after centrifuging (Fig. 9). Given the low density and appearance of OC, it cannot be ruled out OC is decanted, making the samples unfit for data analysis.

Second decalcification method

This second decalcification method is a simplified version of the first decalcification method described above, where decantation of OC is avoided. In the second decalcification method, crushed samples are weighed and decalcified directly in the cups. ±40 mg is added to the cup, after which acid is added to the cup for decalcification. The acid is evaporated at ±60°C. Both ridged silver and smooth tin cups are tested. In the ridged silver cups, three drops of HCl 1M are added. Capillary action likely causes the acid to 'leave' the silver cup, pushing the silver cup out of its tray and making the silver cups unreliable. To avoid capillary action, smooth walled cups should be used. As smooth walled silver cups are unavailable in the appropriate size, tin cups are used instead. To ensure the acid does not dissolve the smooth tin cups, 0.2 ml of 0.5M HCl is used to decalcify the samples. It seems the smooth walled tin cups had no capillary action and did not dissolve, making the tin cups the most reliable option for decalcification.

Elemental Analyzer (EA)

When the samples are decalcified properly, cups are sealed under a pure oxygen airflow to ensure nitrogen signals are not disturbed and are ready for the Elemental Analyzer (Delta-V advantage EA-IRMS). Every run contains the following lab standards, consisting of 500 µg Nicotinamide (only in the first round of standards of each run), a blank cup, a cup of 200 - 2000 µg Acetanilide, a cup of 200 - 2000 µg Atropine and a cup of 30 - 40 mg IVA. Nicotinamide, Acetanilide and Atropine are pure substances, IVA is a soil standard 2. These standards are used to calibrate the Elemental Analyzer to

the correct carbon and nitrogen values. Every run is set up as follows: the first round of standards, followed by 10 decalcified samples, the second round of standards, followed by another 10 decalcified samples, followed by another final round of standards. The first run compared the same six samples using different decalcification methods. After finding the most suitable decalcification method, run 2, 3, and 4 were used for the 59 remaining samples. TOC content is reported in weight percentage (wt%) with an analytical error of generally 1% for each measurement, with one measurement having an analytical error of 6%.

Isotope Ratio Mass Spectometry (IRMS)

After analysis of the TOC data, 20 samples were picked for IRMS. Samples selected for the IRMS are evenly distributed over every vertical section and sub-environment to avoid bias. To give a representative overview of the system, samples were chosen based on an equal distribution of TOC values, where all sub-environments and logs are represented relative to their availability. The second decalcification method without decantation was used to decalcify the samples, similar to the TOC analyses. For the samples to move smoothly through the machine, the foldable ridged silver cups (0.22 ml) should be used for the stable carbon isotope ($\delta^{13}C$) analysis. To avoid capillary action 0.025 ml 18.5% HCl was added twice to decalcify the samples. The aim of the IRMS is to have 50 µg carbon in every cup. The amount of sample added to the cup is based on the TOC values from the Elemental Analyzer. To calibrate the IRMS to the correct $\delta^{13}C$ values, two lab standards were used: Nicotinamice, which has a carbon percentage of 59%, and GQ, which has a carbon percentage of 1.2%. GQ is a lab standard used for $\delta^{13}C$ calibration. This results in the following set up: a round of standards, a round of ten samples, another round of standards, another round of ten samples and a final round of standards. The first round of standards consists of Nicotinamide (50 – 100µg), three blanks, two GQ (2.5 – 6 mg) and another Nicotinamide. The other two rounds with standards contain two GQ cups and one Nicotinamide cup. Stable carbon isotopic values are reported in ‰ Vienna PDB with a maximum analytical error of 0.1‰ on the measurements.

Data processing

All data generated in this research is combined to give a complete overview of OC particle size, origin, and distribution in the studied lobe. Statistical analysis (ANOVA) is used to determine if sub-environments show a significant difference from each other. The particle size and weight percentage are plotted per log and per sub-environment. This is compared to the size distribution of the thin section analysis to explore if the two are connected, and if a thin section analysis may be a good estimate for TOC values. A complete overview is presented in a figure combining the pre-existing logs with the TOC values and the POC size.

Results

Table 1 of the Supplementary materials shows the results of the OC particle analysis, TOC and $\delta^{13}C$ lab analysis as well as the mineral grain size sensu Spychala et al. (2021) per sample with their respective location in the transect.

Organic Carbon particle size analysis

Organic Carbon particle size distributions of 19 lobe axis, 40 lobe off-axis and 6 lobe fringe thin sections were analyzed are displayed in Figure 10 for all samples and in Figure 11 per sub-environment. Weights are added to the datapoints to account for probability. The distribution lines do not reach a density of 0 at the beginning or end because the proportions of the highest and lowest datapoints are not 0. The added weights cause the open ends of the distribution to look more extreme. An unweighted frequency distribution is presented in Figure 1 and 2 of the supplementary materials. The mean particle size of all sub-environments is 2.97 ϕ (σ = 0.62) or 0.16mm (σ = 0.10). The median particle size is 3.03ϕ, with 50% of the samples varying between 3.4 and 2.7 ϕ and 60 samples between 2.2 and 4 ϕ. The lobe axis sub-environment has a mean particle size of 2.81 ϕ (standard deviation σ = 0.51, or mean D = 0.17 mm). This then decreases in the off-axis sub-environment which has a mean particle size of 3.03 ϕ (σ = 0.67, mean D = 0.16 mm), and decreases further in the fringe sub-environment which has a mean particle size of 3.07 ϕ (σ = 0.46, mean D = 0.14). Almost all particle size distributions are variable within a range of ϕ = 0 – 5, ϕ = 5 being close to the cut-off value. Four particle size distributions are bimodal. The axis and off-axis sub-environments are moderately sorted while the fringe sub-environment is well-sorted (Folk and Ward, 1957). Looking at Figure 11, differences between median particle sizes seem minor though existent, however the statistical Analysis of Variance (ANOVA) shows that sub-environments are not statistically different p-value = 0.42, where p < 0.05 indicates a statistical difference between sub-environments with a confidence interval of 95% (Table 1).

Table 1: mean OC particle sizes and standard deviation on φ and mm scale, including ANOVA analyses.

	Mean φ	*σ for φ*	*Mean D (mm)*	*σ for D*
Axis (n=19)	2.81	0.51	0.17	0.078
Off-axis (n=40)	3.03	0.67	0.16	0.11
Fringe (n=6)	3.07	0.46	0.14	0.049
Total	2.97	0.62	0.16	0.10
	F-value:	p-value:	F-value:	p-value
ANOVA	0.88	0.42	0.31	0.73

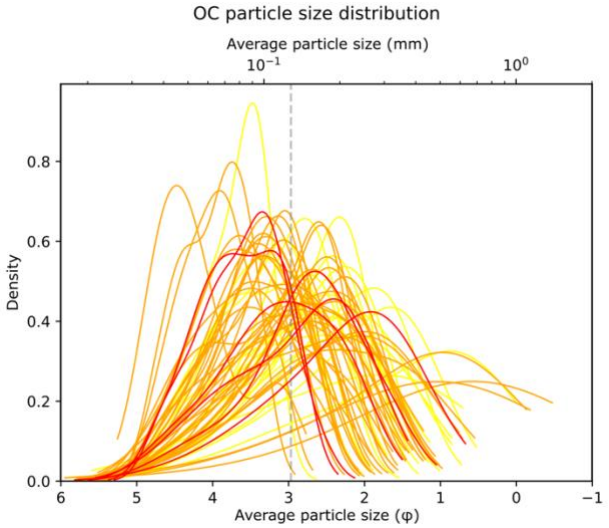

Figure 10: Weighted OC particle size density estimation of the lobe axis, off-axis, and fringe sub-environments of Clinothem 12. Gray line indicates the average particle size. Density plot contains all particles analyzed in the thin sections.

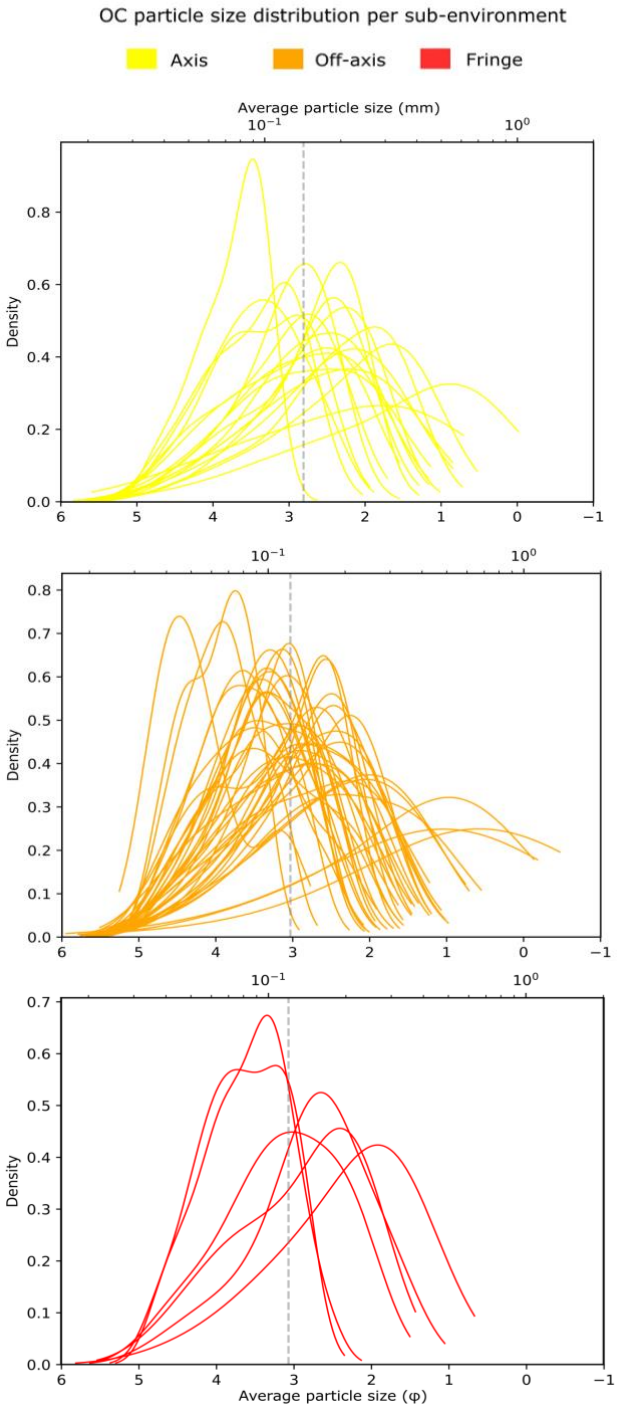

Figure 11: weighted OC particle size density estimations of all particles measured per lobe sub-environment. Gray lines are average of all the thin sections of the sub-environment.

All weighted grains are in a boxplot (Fig. 12), where differences seem more obvious. Figure 13a shows the mean particle size of every thin section over distance. The OC particle sizes in the lobe axis deposits decrease over a distance of 2289m. The OC particle sizes of the off-axis sub-environment deposits are found over the entire distance of the transect, with the exception of the most distal Hyrnestabben log, and particle sizes remain similar. The OC particle sizes of the lobe fringe deposits decrease over the most distal 1083m. All sub-environments have a similar mean particle size of around ϕ = 3 per thin section over distance, also visible in the particle size distributions (Fig. 9). The OC particle sizes of every thin section are plotted next to the existing logs and are shown in Figure 14. Peaks in OC particle sizes are found in the tops and bottoms of the logs, with a typical OC particle size of at least ~ 2.5ϕ. Samples 1 Log 6 (ϕ = 1.54), 5 Log 3 (ϕ = 1.42), and 10 Log 5 (ϕ = 1.27) are all larger than 2ϕ, and only sample (2 Log 2, ϕ = 0.79) is larger than 1ϕ (Fig. 13).

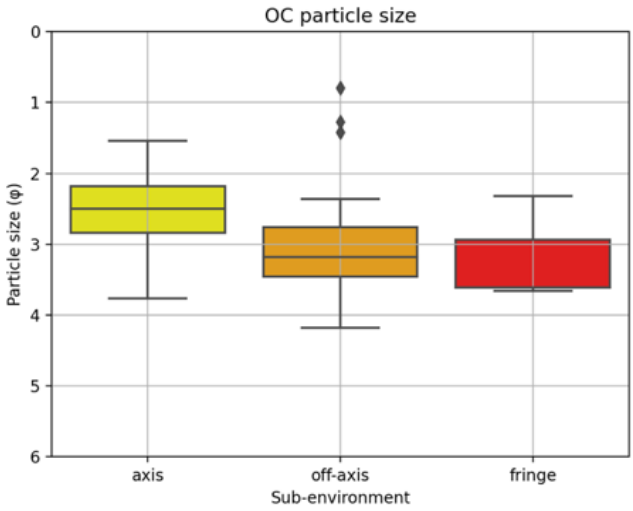

Figure 12: Boxplot showing the weighted mean of all measured organic carbon particles sizes per sub-environment in φ.

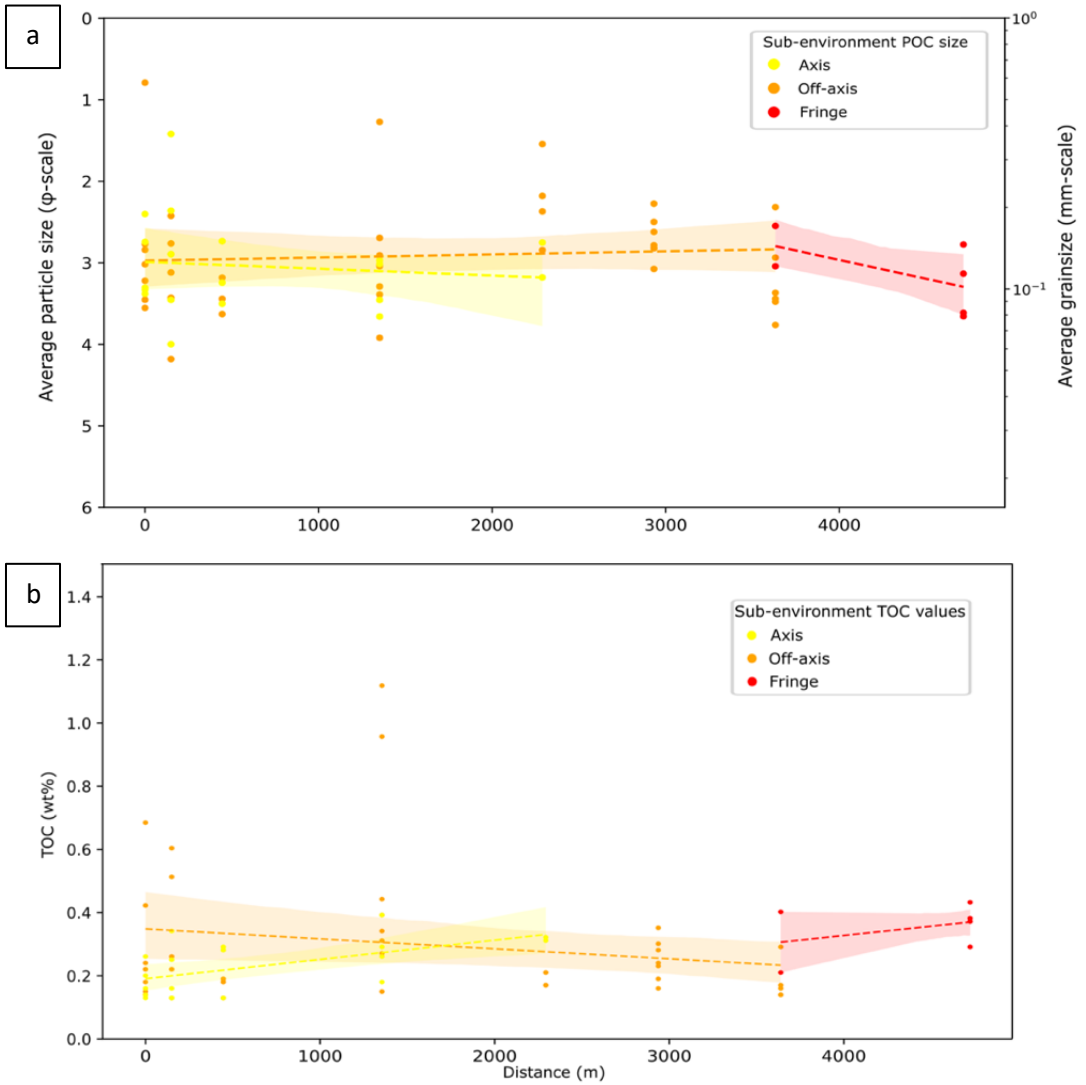

Figure 13: a) Average OC particle size of each thin section plotted over the entire transect, with fitted regression per sub-environment. b) TOC value per sample plotted over the entire transect, with fitted regression per sub-environment.

Total Organic Carbon analysis

Figure 13b shows the Total Organic Carbon values in weight percentage (TOC wt%) over the entire distance of the youngest lobe of Clinothem 12. It shows data of 19 lobe axis, 39 lobe off-axis and 7 lobe fringe samples. Generally, the TOC wt% is between 0.2 and 0.5% and increases towards the distal parts of the lobe complex. Outliers are present in the proximal parts and in the off-

Table 2: Mean TOC wt% and standard deviation values per sub-environment.

	Mean of TOC wt%	*σ of TOC wt%*
Axis (n=19)	0.2	0.08
Off-axis (n=39)	0.3	0.21
Fringe (n=7)	0.4	0.07
Total (n=65)	0.3	0.18
	F-value:	p-value:
ANOVA	1.54	0.22

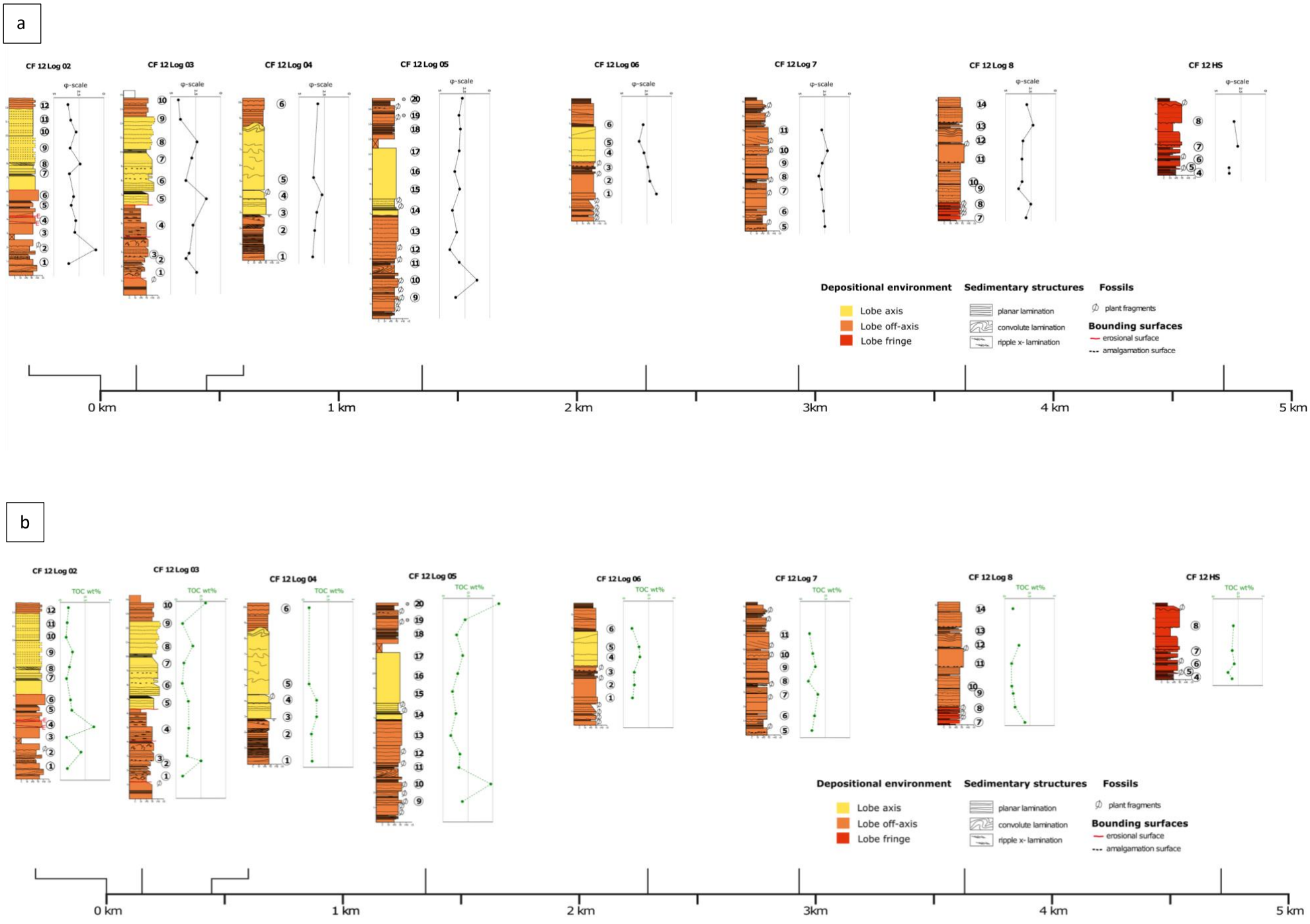

Figure 14: Locations of logs (see also fig. 3C) and sample numbers of the youngest lobe of Clinoform 12. Colours indicate depositional sub-environment. a) OC particle size (φ-scale) plotted next to the corresponding samples. b) TOC (wt%) plotted next to the corresponding samples.

axis sub-environment (Fig. 13, 15). Values with at least double the mean TOC wt% are considered outliers. This becomes even more evident when looking at Figure 15, where all data is presented in a boxplot per sub-environment. The fringe sub-environment has substantially a higher TOC content than the axis sub-environment. The axis sub-environment has a mean TOC wt% of 0.2 (standard deviation σ: 0.08), off-axis has a mean TOC wt% of 0.3 (σ: 0.21), and the fringe has a TOC wt% of 0.4 (σ: 0.07). However, Analysis of Variance (ANOVA) shows that there are no statistical differences between the sub-environments with p-value = 0.22, where $p < 0.05$ indicates a statistical difference between sub-environments with a confidence interval of 95%.

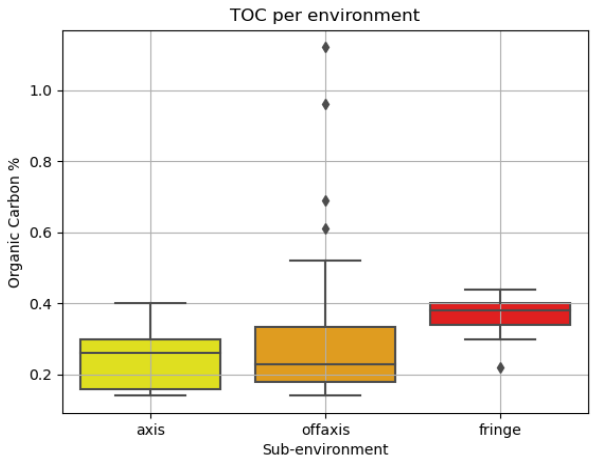

Figure 15: Boxplot showing the average TOC wt% per sub-environment.

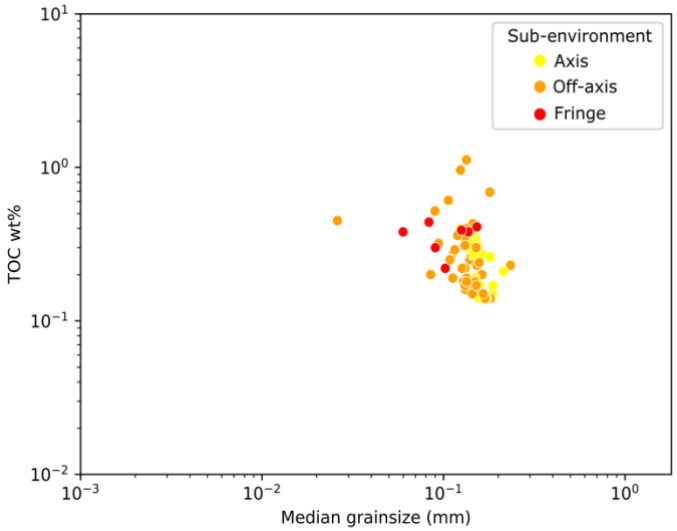

Figure 16: Plot showing the relationship between TOC (wt%) and sedimentary grain size fraction of mineral sand as presented in Spychala et al. (2021).

While the TOC wt% in the lobe axis and fringe increase with distance, the TOC wt% decreases over distance in the off-axis sub-environment (Fig. 13b). The lobe axis sub-environment increases in TOC from an average of 0.2wt% at 0m to 0.3wt% at its furthest sample at 2289m. The off-axis sub-environment decreases in TOC from an average of 0.3wt% at 0m to 0.2wt% at 3632m. The fringe sub-environment increases in TOC from an average of 0.3wt% at 3632m to 0.4wt% at 4715m, though it only has two sample locations.

The TOC values are plotted against the mineral grain size sensu Spychala et al. (2021) in Figure 16. Here, we see that TOC wt% seemingly increases with a smaller median grain size, though the fanning distribution on a logarithmic scale looks more like a cloud. This is largely due to the small range of mineral grain sizes and TOC content of the data. The Total Organic Carbon (TOC wt%) of every sample is plotted next to the existing logs (Fig. 14). Peaks in TOC content are found in the tops and bottoms of the logs, with TOC values nearing or surpassing 0.5%. Samples 2 (0.52%) and 10 (0.61%) of Log 3, 4 Log 2 (0.69%), and 10 Log 5 (0.97%) surpass a TOC value of 0.5%, and sample 20 Log 5 (1.12%) has a higher TOC value than 1% (Fig. 13). Furthermore, TOC values increase with distality and is higher in the off-axis to fringe sub-environments.

Stable carbon isotope analysis

Figure 17 shows the stable carbon isotopic values ($\delta^{13}C$, ‰ Vienna PDB) of the OC in 20 samples. The samples used for this analysis are evenly distributed over the entire distance of the youngest lobe of Clinothem 12, with 6 samples from the lobe axis, 12 samples from the lobe off-axis and 2 from the lobe fringe. Figure 18 shows the $\delta^{13}C$ values of the samples at the locations the samples were taken. $\delta^{13}C$ values decrease as TOC values increase and have distinct values for each sub-environment (Fig. 17a). The lobe axis sub-environment contains the heaviest $\delta^{13}C$ values. The average $\delta^{13}C$ value for the lobe axis sub-environment is -20.9‰ with all values between -19 and -23‰, the lobe off-axis shows an average value of -22.1‰ with the widest distribution of values between -20 and -25‰, and the lobe fringe shows an average value of -23.7‰ with only two values of -23.6 and -23.9‰. The $\delta^{13}C$ values seem unrelated to OC particle size (Fig. 17b) or distance (Fig. 18), as not enough samples have been measured to see a clear trend over the entire transect.

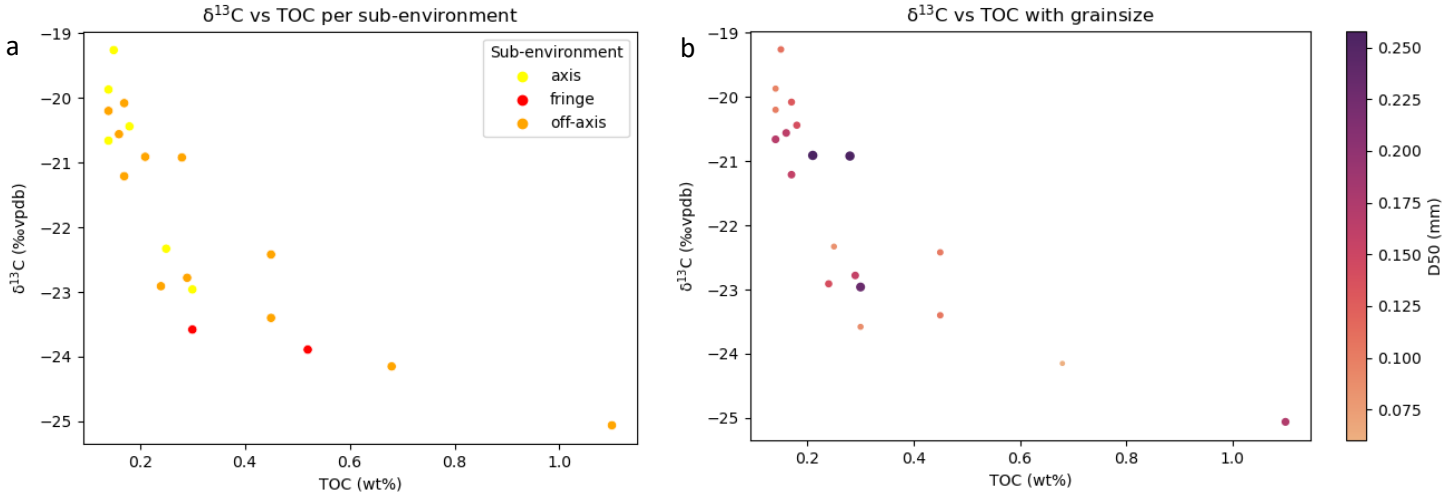

Figure 17: $\delta^{13}C$ values plotted against TOC values. a) shows sample values per sub-environment, b) shows sample values with corresponding median OC particle size.

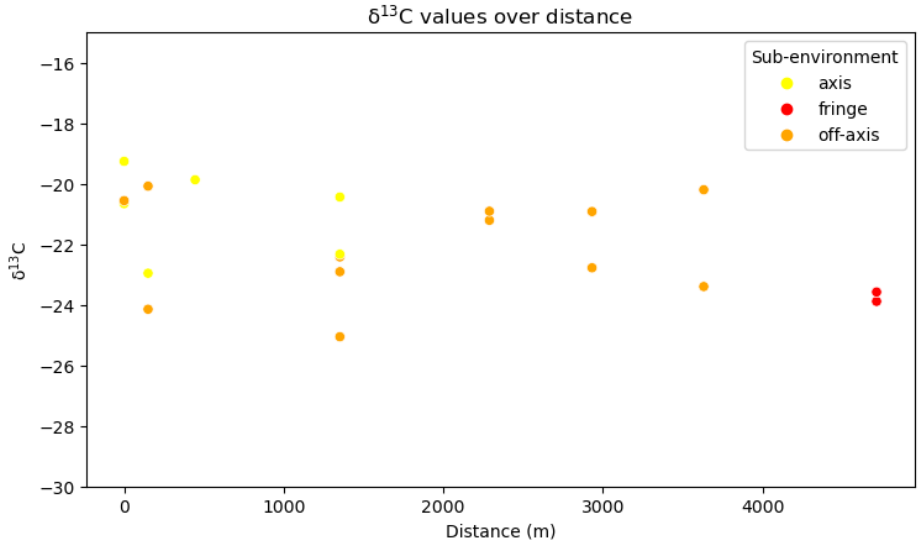

Figure 18: $\delta^{13}C$ values plotted over the distance of the entire transect.

Discussion

Organic Carbon burial

Particulate Organic Carbon distribution

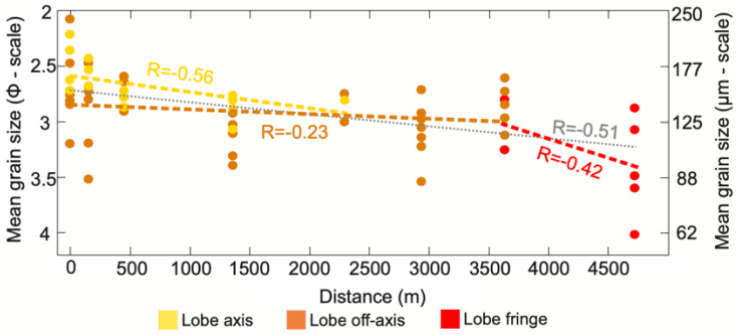

Figure 19: Mean mineral grain sizes over the transect of the lobe (Spychala et al., 2021).

The distribution of POC indicates the physical behaviour of OC particles in the turbidite lobe. When comparing the OC particle sizes to the mineral grain sizes reported by Spychala et al. (2021) (Fig. 19), a similar trend of decreasing OC particle and mineral grain size over the distance of the transect is visible, though the OC particle sizes are smaller at around 3ϕ. That same trend seems to be represented in the sub-environments of the lobe. However, despite the variability in the Organic Carbon particle distributions (Fig. 10, 11, Table 1), there is no statistical difference between sub-environment groups of the youngest lobe of Clinothem 12. Both the mineral grain sizes and the OC particle sizes decrease slightly basinward, with the coarsest OC particles in the most proximal area of the turbidite. It should be noted that while there is a general decrease over distance, this is only true for the axis and fringe sub-environments. The off-axis sub-environment OC particle size remains within the same range over distance, again much like the mineral grain size trend in Spychala et al. (2021). The decrease in OC particle size (as well as mineral grain size) is likely due to hydrodynamic sorting. Several studies cite hydrodynamics as the primary control on the distribution of organic matter or OC particles in marine environments (Boulter and Riddick, 1986; McArthur et al., 2016; Tyson and Follows, 2000; Van der Zwan, 1990). The reason the off-axis sub-environment does not decrease over distance is due to rapid deposition of the coarsest mineral sand grains in the axis sub-environment, after which the mineral grain sizes are homogeneously distributed and deposited in the off-axis portion of the lobe. This is then followed by the deposition of the finest fraction of the mineral sand in the fringe sub-environment (Spychala et al., 2021). It is assumed that OC particles follow this same principle.

McArthur et al. (2016) discuss the distribution of OC in the Eocene to Oligocene Gres d'Annot deposits, in which a trend of decreasing particle size over distance is also represented in silt to medium sand grain size fractions. McArthur et al. (2016) have no reports on the connection between mineral sand grain size and OC particle size. Hydrodynamic sorting explains the trend of the decreasing OC particle sizes in both the data of this thesis and the data from McArthur et al. (2016), but it does not explain how small particles with a low density end up in mineral sand with a similar or even bigger grain size. OC particles studied in this thesis seem randomly distributed throughout the deposit, whereas OC particles typically are found in the finer fractions of turbidites, as they are lighter than sand. The particles settle as suspended matter, representing the lowest-density fraction of turbidity currents (McArthur et al., 2016). This might not be visible on the scale of a lobe such as the one from Clinothem 12, due to the many turbidites the lobe consists of and the consequent reworking of sediment. Moreover, density and particle size have similar effects on settling velocity, which is used as the guiding physical aspect of deposition of the sediment grains. Fluid mechanics in turbidites requires the OC particles to be much bigger than they are in our dataset to compensate for the low density of OC compared to mineral sand (Kneller and Buckee, 2000). Furthermore, Sparkes et al. (2015) proposed

that the deposition and consequent burial of OC particles might have been achieved by waterlogging OC particles to increase its density. However, even with increased density due to waterlogging, it seems highly unlikely that OC reaches a similar density to mineral sand, raising the question why the OC particles have similar or smaller maximum grain sizes to the mineral sand in the largest grain size fraction, and are randomly distributed in the Clinothem 12. The presence of OC particles in coarse sand with similar grain sizes could be explained by the fact that the OC particles are compared to a mean mineral grain size, while various mineral grain sizes are distributed throughout all sub-environments of the deposit. The mean mineral grain size is similar or bigger than OC particles, but much more fine-grained material, such as silt, is also present. If silt is deposited, larger OC particles with a similar settling velocity to small silt particles should also be able to precipitate. While this principle is visible throughout the entire transect, it does not explain why there are no OC particles present in the proximal area that are larger than mineral sand grains and have a similar settling velocity.

Total Organic Carbon distribution

The Total Organic Carbon content and distribution is important to determine the sequestering potential of turbidite systems. TOC values show a general basinward increase from 0.2 to 0.3 wt%, with the exception of the trend in the off-axis sub-environment, making it the opposite of the OC particle size distribution (Fig. 13, Table 2) and mineral grain size distribution (Fig. 20). The inverse relationship between TOC content and both OC particle and mineral grain size can be explained by hydrodynamic sorting. As mentioned in the Particulate Organic Carbon chapter, hydrodynamic sorting seems to be the primary control on the distribution of organic matter or OC particle sizes in marine environments. Additionally, hydrodynamic sorting causes a basinward increase in TOC content as a result of a decrease in mineral grain size. Due to the low density of OC, settling velocity of OC particles resembles the finer-grained mineral sand fraction that is deposited downstream. OC particles are therefore deposited in an increasing manner in the finer fractions of the lobe as the density of the turbidity current decreases. Another explanation of the inverse relationship between TOC content and both OC particle and mineral grain size is the notion that OC is preferentially adsorbed to finer-grained sediment due to the higher sediment surface area (Paradis et al., 2023). While the grain size still falls in the classification of fine sand and matrix fraction is unknown, organomineral protection in clay could be influencing the preservation of a small portion of the OC in the more distal, fine-grained sediments of the lobe. Organomineral protection prevents degradation of organic matter in sediment (Aufdenkampe et al., 2011; Hedges and Keil, 1995). However, more research towards the matrix of the samples is needed to support this claim.

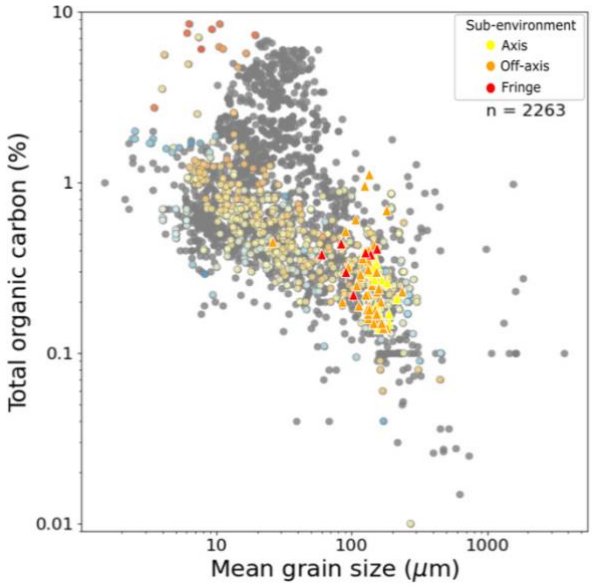

Figure 20: TOC % plotted against the mean grain sizes, compilation of 2263 marine sediment datapoints from Paradis et al. (2023), overlain by the data presented in this thesis in yellow, orange, and red triangles, sorted by sub-environment.

Paradis et al. (2023) performed a metastudy of literature on OC burial in marine sediments. The data presented in this thesis fits the figure from Paradis et al. (2023) (Fig. 18). This relationship of increasing

TOC content with decreasing mineral grain size is in line with several other studies (Hage et al., 2020; Stetten et al., 2015), indicating that turbidite systems behave like any other marine system. More importantly, organic matter can be preserved because of several mechanisms, such as organomineral protection, permafrost, anaerobic zones and rapid burial (Fisher et al., 2018), of which the latter seems the most important in our system. The deposits in Clinothem 12 display an immature character with the presence of shale fragments and poor sorting, which suggests rapid deposition from the shelf-edge (Grundvåg and Helland-Hansen, 2021; Plink-Björklund and Steel, 2004). The rapid deposition and burial rates in the turbidite lobe are what sets turbidite data apart from the data of other marine sediments (Fig. 20). Rapid burial in the lobe prevents degradation of OC by shielding both labile and refractory the OC from oxidation, creating a high OC preservation potential (Galy et al., 2007; Kao et al., 2014). The protection against oxidation depends on the thickness and character of the overlying unit, as increased thickness and mud content would form a stronger protection layer (Hage et al., 2020). Doerner et al. (2020) found pyrite as evidence for sulphate reduction in the Battfjellet Formation and neighbouring deposits, indicating that initial TOC burial values were likely higher but not preserved. While the data presented in this thesis fits the data from marine systems (Paradis et al., 2023), specific turbidite values presented in literature show wide ranges and are difficult to compare. The preserved TOC of 0.29% in the sand-dominated lobe of Clinothem 12 compares to for example 0.2% of preserved TOC in coarse turbidites in the current Ganges Brahmaputra system (Lee et al., 2019), or 3.5% in the muddy, distal Congo lobe (Baudin et al., 2017; Stetten et al., 2015). The sandy Eocene turbidite lobe had a different lobe size and catchment area from the currently active Congo or Ganges Brahmaputra turbidite system, nor is there a lot of quantitative data on other different lobe complexes. This problem highlights the importance of quantitative OC studies in different types of turbidites.

Stable carbon isotopic composition

The stable isotopic composition of the OC can be used to make a distinction between marine and terrestrial OC, which is used to reconstruct the path and depositional system of the analyzed organic matter. The $\delta^{13}C$ values presented in Figures 17 and 18 show that the isotope fractionation becomes more negative over distance and per sub-environment, with the average lobe axis sub-environment value being -20.9‰, the lobe off-axis sub-environment -22.1‰, and lobe fringe -23.7‰. During the majority of the Eocene, the terrestrial end member of $\delta^{13}C$ is -23.4‰, while the marine end member

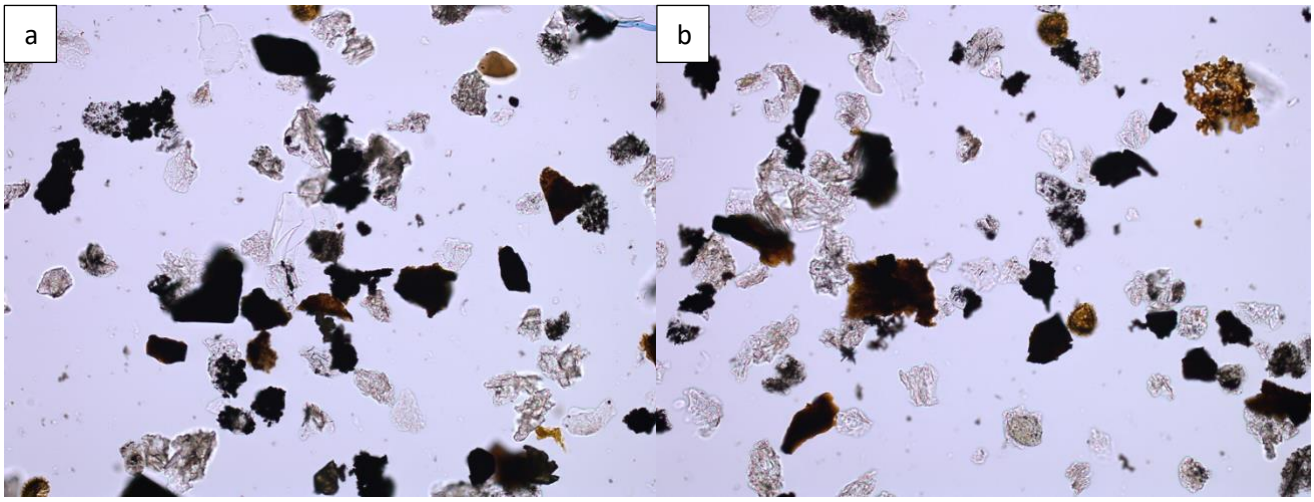

Figure 21: microscopic image (20x magnification) of the charred plant material in the Battfjellet Formation, from a) sample 2, log 6 and b) sample 7, log 2. Similar characteristics such as colour and shape indicate entire deposit experienced the same pressure and temperature conditions (H. Brinkhuis, personal communication, December 21, 2023).

is -27.4‰ (Sluijs and Dickens, 2012). Based on microscopic analysis of OC particles, the material found in Clinothem 12 seems charred (Fig. 21, H. Brinkhuis, personal communication, December 21, 2023). The end member of the burnt equivalent of OC would be ~2‰ less negative than aforementioned end members (Bird and Ascough, 2012), meaning that charred terrestrial material in our case would have an end member of around -21‰, or that the initial $\delta^{13}C$ values of our samples were ~2‰ more negative. Moreover, a lack of iron and the presence of pyrite as a result of microbial organic matter degradation is stated as the indicator for sulphate reduction (Doerner et al., 2020). Sulphate reduction has degraded labile organic matter, causing an additional shift of several permille in stable carbon isotopic values of the samples by making the isotope fractionation more negative (Doerner et al., 2020). $\delta^{13}C$ values in Figure 17 and 18 together with microscopic analysis of OC particles of Figure 21 indicate that the proximal deposits of the lobe likely consist of charred biogenic terrestrial matter. However, it cannot be ruled out that brown or opaque minerals such as hematite or pyrite are present. Charring likely happened due to thermal metamorphosis when the entire deposited experienced the same pressure and temperature path after burial (Fig. 21, H. Brinkhuis, personal communication, December 21, 2023), though other options, such as charring from forest fires, cannot be ruled out. The terrestrial input is dominant in the lobe axis and off-axis sub-environments, while the more distal, lobe fringe deposits show an increasing marine influence with more negative OC isotopes (Fig. 17, 18).

Marine Organic Matter accumulates on the slope bed between turbidity currents, the MOM would then be entrained by the turbidity during an event (Fig. 22). This mechanism also works for hyperpycnal flows directly depositing sediment onto the slope. Additionally, slumping can mix the terrestrial matter with slowly accumulated marine matter and deposit it down the transect of the lobe (Sparkes et al., 2015). The entrained and mixed in MOM would naturally increase down the slope, compared to the more dominant terrestrial matter in the proximal deposits (Fig. 22). This also results in the increase of TOC wt% down the transect. The organic material is picked up from the slope and deposited further down slope where the OC accumulates, which is in line with other reports of increasing TOC values with increasing marine OC input (McArthur et al., 2016; Yedema et al., 2023). Interestingly, the presence of generally more labile marine OC indicates that rapid burial in the lobe prevents the degradation of labile OC to some extent (Talling et al., 2024). Stetten et al. (2015) found well preserved plant material in the distal parts of turbidites, indicating that turbidity currents are able to transport terrestrial matter to the fringe sub-environment. Reports of OC particles indicate that it is not uncommon to find fossil leaves, wood, or coal in sandy turbidites (Lee et al.,

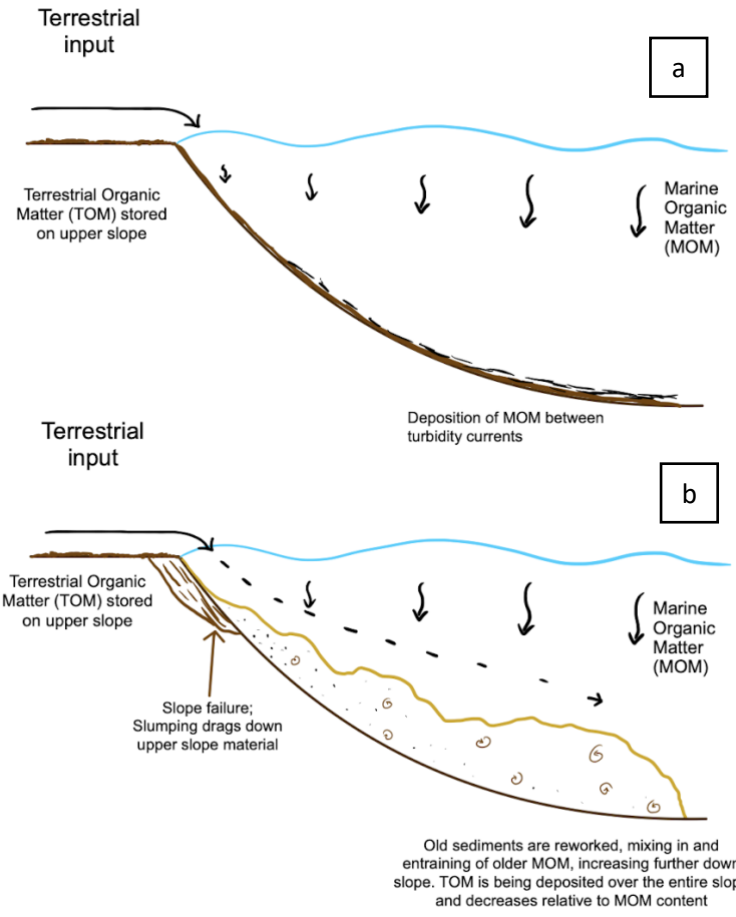

Figure 22: a) A period of non-deposition of turbidites, where MOM from the water column is deposited on the slope. b) Turbidity current, reworking the material deposited on the slope and mixing in the upper slope material.

2019; Saller et al., 2006), which in line with the terrestrial isotope fractionation and plant fragments found in our lobe deposits.

Source, path, and budget of Organic Carbon

Source and path

The source of the terrestrial OC is not as straightforward as the marine OC that has settled from the water column. Based on previous literature (Grundvåg et al., 2023; Helland-Hansen and Grundvåg, 2021; Petter and Steel, 2006; Plink-Björklund and Steel, 2004) and the abundance of terrestrial OC, it is likely that the lobe is fed by a hyperpycnal flow. The progradational nature of the sediments indicates that hyperpycnal flows deposited large amounts of organic rich sediments directly onto the slope and basin floor, or on the upper slope where it was stored (Grundvåg and Helland-Hansen, 2021). Subsequent slope failure, as a result of a drop in sea-level, caused gravity triggered slide and slump deposits, dragging the organic rich sediments down the slope (Grundvåg et al., 2023). A similar mechanism has been identified on the Corsica-Sardinia Massif, describing currents, local vegetation and oxygenation as important factors to deliver organic matter to turbidite systems (McArthur et al., 2016). Furthermore, the large influx of sediments and immature character of the sediments indicate rapid burial rates (Grundvåg and Helland-Hansen, 2021; Plink-Björklund and Steel, 2004), creating the high preservation potential that Clinothem 12 needed.

The direct source of the OC in the lobe seems to be terrestrial biogenic material supplied by hyperpycnal flows, which is either stored on the upper slope and then slumped or directly deposited onto the basin floor. The fluvial input in the hyperpycnal flow carries soil and plant material that is largely supplied by floods. Clare et al. (2017) have reported that high river discharge as a result of flooding, combined with increased sedimentation rates, can result in delta front failure, which Grundvåg et al. (2023) described as the most likely mechanism depositing the sediment found in Clinothem 12. The sediments are then deposited on the slope. Together with the visual analysis of microscopic images of the OC in the deposits, this would make the probable source of the terrestrial OC in Clinothem 12 the plant and soil material that is stored on the delta front, which is also found in the Aspelintoppen Formation. This is in line with Doerner et al. (2020), who claim that both the Battfjellet and the Aspelintoppen Formations are the same pollen/spores and leaf material. Ultimately, the entire deposit and its organic content likely has been compacted and thermally metamorphosed to a point where (char)coal was able to form, which is not unlikely considering the presence of thin coal layers at the base of the Aspelintoppen Formation (Dallmann, 2015).

Budget

This Organic Carbon budget serves as a tool to determine what sets turbidites apart from other marine sediments. To calculate an OC budget, the size of the lobe and density of the sediment in the lobe should be considered. The thickness of the youngest lobe of Clinothem 12 is measured to be 15m (Spychala et al., 2021), which corresponds to a lobe width of around 10.5km based on the morphometrics of unconfined lobes (Prélat et al., 2010; Prélat et al., 2009). Crabaugh and Steel (2004) have reported the sandy basin-floor fans to be no longer than 12km, which is used here for the OC budget of the sandy part of the lobe. They estimate the entire fan to be 30km long maximum, which is used for the estimated budget of the entire lobe. Furthermore, the density of the rock in the lobe is estimated to be 2300 kg/m based on the mineral composition and minimal porosity of the sandstones.

The porosity of the rock is disregarded in this budget estimate due to compaction of the sediment. This results in the following calculations for sandy part of the lobe and the entire lobe respectively:

$$V_{sandy\ lobe} = thickness\ \cdot\ length\ \cdot width = 15\ \cdot\ 12\ 000\ \cdot 10500 = 1.89e9\ m^3$$
$$W_{sandy\ lobe} = V_{sandy\ lobe} \cdot \rho\ = 1.89e9 \cdot\ 2300 = 4.35e12\ kg\ sediment$$
$$W_{OC-sandy\ lobe} = W_{sandy\ lobe} \cdot TOC\ = 4.35e12 \cdot\ 0.0029 = 1.26e10\ kg\ OC$$

$$V_{entire\ lobe} = thickness\ \cdot\ length\ \cdot width = 15\ \cdot\ 30\ 000\ \cdot 10500 = 4.73e9\ m^3$$
$$W_{entire\ lobe} = V_{entire\ lobe} \cdot \rho\ = 4.73e9 \cdot\ 2300 = 1.09e13\ kg\ sediment$$
$$W_{OC-entire\ lobe} = W_{entire\ lobe} \cdot TOC\ = 1.09e13 \cdot\ 0.0029 = 3.15e10\ kg\ OC$$

Accumulation rates play a major part in the sequestration potential of the lobe. Clinothem 12 is estimated to be deposited with a 100kyr cyclicity that is influenced by climate and sea-level change (Steel and Olsen, 2002). It is therefore assumed in this thesis that the lobe complex is deposited over a time that is at maximum similar to the 100kyr cyclicity. The entire lobe complex studied in Spychala et al. (2021) consists of two lobes, one of the lobes is thus deposited with a cyclicity of maximum 50kyr. However, the time constraints on the regressive megasequence of the Gilsonryggen Member, Battfjellet Formation and Aspelintoppen Formation as a whole are very clear, and Grundvåg and Helland-Hansen (2021) estimate in unpublished work that the units underlying Clinothem 12 required more time to deposit than previously mentioned. Therefore, they assume that the timespan over which Clinothem 12 has been deposited is less than 100kyr, but no specific assumptions are made. While the Clinothem was deposited over a less-than-100kyr cycle, it is highly unlikely that the lobes of the lobe complex were deposited over the entire duration of the cycle. Additionally, the period of activity for the short-lived turbidity currents likely only falls within a section of the 100kyr sea-level change cycle, further shortening the period of deposition. The shorter timeframe makes the estimated OC budget for the maximum 50kyr of both the sandy part of the youngest lobe as well as the entire youngest lobe an underestimation and an average over the cyclicity of the clinoform formation. Since it is impossible to know the true timeframe over which the youngest lobe was deposited, the maximum timespan of 50kyr is used, over which the OC content is averaged. The weight of OC in the sandy, 12 km long part of the youngest lobe is 12.6 Tg, which results in a preservation potential of at least 252126 kg OC/yr, or 2.5 $\cdot 10^{-4}$ Tg OC/yr, corresponding to an accumulation rate of 50kyr. The sandy part of the youngest lobe is deposited over 126 km^2, which results in an OC budget of 2001 kg OC/km^2/yr. Preservation potential increases significantly when the accumulation rate is changed to 40kyr. Assuming a faster accumulation rate of 40kyr for the youngest lobe, results in a vast increase in preservation potential to 315158 kg OC/yr, or 2501 kg OC/km^2/yr.

The weight of the OC in the 30 km long, entire youngest lobe is 31.5 Tg, which results in a preservation potential of at least 630315 kg OC/yr, or 6.3 $\cdot 10^{-4}$ Tg OC/yr assuming an accumulation rate of 50 kyr. The entire youngest lobe is estimated to be 315 km^2, but the OC budget per km^2 of course remains the same as in the sandy part of the lobe. Assuming the same increase accumulation rate of 40kyr, the preservation potential increases to 787894 kg OC/yr. The budget of the entire youngest lobe is likely an underestimate, as the most distal parts of the lobe would consist of more mud- and clay-rich material. This increases the influence of hydrodynamic sorting, the sediment surface area, and organomineral protection potential, resulting in increased TOC values.

Quantifying the OC budget in the youngest lobe of Clinothem 12 comes with several uncertainties. In the case where net atmospheric CO_2 sequestration would be quantified, knowledge of the amount of petrogenic (coal, sediments) versus biogenic (plants, soil) OC is required (Galy et al., 2007; Sparkes et al., 2015). Since there is no distinction between petrogenic in the form of previously sequestered biogenic material and new biogenic material, this OC budget is an overestimation for net CO_2 uptake from the atmosphere. On the other hand, this OC budget is an underestimation of the initial TOC sequestering capabilities of sandy turbidites due to the reported sulphate reduction of labile OC (Doerner et al., 2020). This estimate thus shows the budget of the OC that is preserved on a geological timescale.

What sets this turbidite lobe apart from other marine systems (Fig. 20) are the different accumulation and burial rates (Fig. 23). Assuming the differences in sediment accumulation rates between different deposits are similar in the Battfjellet Formation compared to the Congo system in Figure 23, sediment accumulation rates are up to five orders of magnitude larger than other deposits outside the fan, also near the coastline (Talling et al., 2024). This high sedimentation rate is in line with the previously suggested rapid burial, indicated by the immature character of the deposits. Rapid burial of OC leads to a burial efficiency of 60 – 100% in turbidites, where other marine sediments have a burial efficiency of 10 – 45% (Talling et al., 2024). Where OC is more easily degraded in other marine sediments, the thick layer of rapidly deposited sediment shields the OC in turbidite lobes from degradation on a geological timescale. Rapid burial prevents the labile marine OC present in the lobe to be degraded and released back into the atmosphere, increasing the potential of turbidite lobe as a sink for atmospheric CO_2 (Talling et al., 2024).

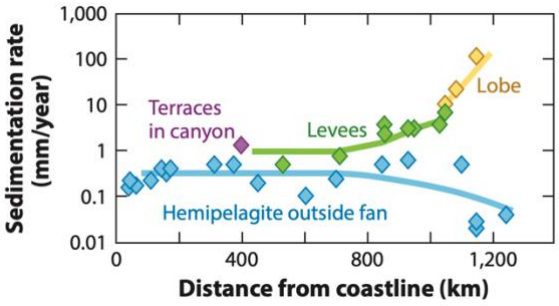

Figure 23: Sediment accumulation rates in different types of deposits of the Congo submarine fan (Talling et al., 2024).

When comparing our estimated preserved OC budget of 2.5 $\cdot 10^{-4}$ Tg OC/yr (2001 kg OC/km^2/yr), it is clear that our budget is much smaller than large scale modern systems, even when assuming a much shorter period of deposition. For example, 0.4 Tg POC/yr is buried in the Congo lobe complex of 3000 km^2 (Rabouille et al., 2019; Stetten et al., 2015), which equals 133 333 kg POC/km^2/yr. Kao et al. (2014) report a total budget of 1.4-1.7 Tg OC/yr in sandy marine deposits of offshore Taiwan during a typhoon. Comparing the data from this thesis to active systems seems redundant: they differ in composition, catchment area, scale, sedimentation rate, and even the amount of OC that can be buried might be different, as atmospheric pCO_2 fluctuates on the geological timescale. A lack of precise time constraints of the duration of deposition in Clinothem 12 makes an accurate OC budget even more challenging to create. The submarine fan system from the Central Tertiary Basin, which Clinothem 12 belongs to, consists of several small fans along the margin of the basin, that are each individually fed by small-scale streams through hyperpycnal flows (Grundvåg et al., 2023). In contrast, the Congo submarine fan is incredibly well constrained, it is one of the largest submarine fans in the world and is fed by the second largest river on the planet that is currently active (Stetten et al., 2015). Developing a method to integrate all sediment input of the submarine fans in the Central Tertiary Basin into the basin would allow for a more accurate comparison between our system and other systems, as well as enabling an improved comparison between differently scaled fan systems in general. To effectively compare OC sequestering and preservation potential in turbidites, further

quantitative research is needed on a wide variety of turbidites in time. Furthermore, the ability to distinguish between petrogenic OC and biogenic OC would give a much clearer view on atmospheric CO_2 sequestration, however this seems impossible on geological timescales.

Conclusions

The sandy upper lobe of Clinothem 12 of the Battfjellet formation poses as an excellent research area to analyze how turbidity currents function as a carbon sink in the preservation of Organic Carbon on geological timescales. OC particle analysis indicate that OC particles follow a similar trend to mineral grain size, which is dictated by hydrodynamic sorting. However, the mechanism of hydrodynamic sorting in this context remains unclear, warranting further research. TOC analysis showed that previously measured mineral grain size likely dictates the TOC content. The TOC content increase towards the end of the turbidite where mineral grain size decreases, which is likely also dictated by hydrodynamic sorting. Stable carbon isotope analysis reveals that the OC in Clinothem 12 is a mixture series that shows terrestrial dominance in the proximal areas and becomes increasingly more mixed with a marine signal towards the fringe sub-environment. Terrestrial material is stored on the shelf through hyperpycnal flows, after which it is deposited on the slope following delta front failure. Due to the high sedimentation rates of the hyperpycnal flows and consequent delta front failure, the burial rate of the OC is high. This results in a flux of at least 252126 OC/yr in a small lobe of 126 km^2, or 2001 kg OC/km^2/yr. While the amount sequestered in Clinothem 12 seems insignificant on a global scale, turbidites seemingly sequester similar amounts of OC to other marine deposits when looking at mean mineral grain sizes. Combining these TOC contents with the rapid burial rates in turbidites, the deposits have impressive OC preservation potential on a global scale and geological timescale. Moreover, rapid burial prevents labile carbon to be released back in into the atmosphere, making it a significant sink of atmospheric CO_2. A lack of carbon budgets in similar deposits (sandy turbidites, Eocene deposits) makes it difficult to put our data in an Eocene carbon cycle framework. Time constraints of turbidite deposits need to be improved and more turbidite lobe complexes need to be evaluated. Additional quantitative research would also aid in solving the puzzle that is the Eocene carbon cycle. This is a small step towards an improved Eocene carbon cycle model and more research is required to give insight of what remains unknown.

Acknowledgements

Firstly, I would like to thank my supervisors, Joris Eggenhuisen and Francien Peterse for their guidance, discussions, and for sharing their passion and insights. I thank Henk Brinkhuis for his discussions and insight on the palynology slides. I would also like to thank Mateus Kroth and Pelle Adema for their help with data analysis in Python. I thank Leonard Bik, Desmond Eefting, Giovanni Dammers, and Natasja Welters for their help in the lab. Lastly, thank you to Yvonne Spychala, Florian Pohl, and Sten-Andreas Grundvåg for retrieving the samples during the fieldwork on Svalbard.

References

Aufdenkampe, A.K., Mayorga, E., Raymond, P.A., Melack, J.M., Doney, S.C., Alin, S.R., Aalto, R.E. and Yoo, K. (2011) Riverine coupling of biogeochemical cycles between land, oceans, and atmosphere. *Frontiers in Ecology and the Environment*, **9,** 53-60 DOI: https://doi.org/10.1890/100014.

Baudin, F., Stetten, E., Schnyder, J., Charlier, K., Martinez, P., Dennielou, B. and Droz, L. (2017) Origin and distribution of the organic matter in the distal lobe of the Congo deep-sea fan – A Rock-Eval survey. *Deep Sea Research Part II: Topical Studies in Oceanography*, **142,** 75-90 DOI: https://doi.org/10.1016/j.dsr2.2017.01.008.

Bergh, S., Braathen, A. and Andresen, A. (1997) Interaction of basement-involved and thin-skinned tectonism in the Tertiary fold-thrust belt of central Spitsbergen, Svalbard. *Aapg Bulletin - AAPG BULL*, **81,** 637-661.

Bianchi, T.S. and Bauer, J.E. (2011) 5.03 - Particulate Organic Carbon Cycling and Transformation. In: *Treatise on Estuarine and Coastal Science* (Eds E. Wolanski and D. McLusky), pp. 69-117. Academic Press, Waltham.

Bird, M.I. and Ascough, P.L. (2012) Isotopes in pyrogenic carbon: A review. *Organic Geochemistry*, **42,** 1529-1539 DOI: https://doi.org/10.1016/j.orggeochem.2010.09.005.

Boulter, M.C. and Riddick, A. (1986) Classification and analysis of palynodebris from the Palaeocene sediments of the Forties Field. *Sedimentology*, **33,** 871-886 DOI: https://doi.org/10.1111/j.1365-3091.1986.tb00988.x.

Braathen, A. and Bergh, S.G. (1995) Kinematics of Tertiary deformation in the basement-involved fold-thrust complex, western Nordenskiøld Land, Svalbard: tectonic implications based on fault-slip data analysis. *Tectonophysics*, **249,** 1-29 DOI: https://doi.org/10.1016/0040-1951(95)00036-M.

Burdige, D.J. (2007) Preservation of Organic Matter in Marine Sediments: Controls, Mechanisms, and an Imbalance in Sediment Organic Carbon Budgets? *Chemical Reviews*, **107,** 467-485 DOI: 10.1021/cr050347q.

Charles, A.J., Condon, D. J., Harding, I. C., Pälike, H., Marshall, J. E. A., Cui, Y., Kump, L., and Croudace, I. W. (2011) Constraints on the numerical age of the Paleocene-Eocene boundary. *Geochem. Geophys. Geosyst.*, **12** DOI: 10.1029/2010GC003426.

Clare, M., Talling, P., Cartigny, M., Pratomo, D. and Clarke, J. (2017) *Preconditioning and triggering of offshore slope failures and turbidity currents revealed by most detailed monitoring yet at a fjord-head delta*.

Clifton, A.J. (2012) *The eocene flora of Svalbard and its climatic significance*, University of Leeds.

Crabaugh, J.P. and Steel, R.J. (2004) Basin-floor fans of the Central Tertiary Basin, Spitsbergen: relationship of basin-floor sand-bodies to prograding clinoforms in a structurally active basin. *Geological Society, London, Special Publications*, **222,** 187-208 DOI: doi:10.1144/GSL.SP.2004.222.01.10.

Dallmann, W.K. (2015) *Geoscience atlas of Svalbard*. Norsk polarinstitutt.

de Leeuw, J. (2017) *The sedimentary record of submarine channel morphodynamics*, UU Dept. of Earth Sciences.

Doerner, M., Berner, U., Erdmann, M. and Barth, T. (2020) Geochemical characterization of the depositional environment of Paleocene and Eocene sediments of the Tertiary Central Basin of Svalbard. *Chemical Geology*, **542,** 119587 DOI: https://doi.org/10.1016/j.chemgeo.2020.119587.

Ferreira, T. and Rasband, W. (2012) ImageJ User Guide, IJ 1.46r, **2023**.

Fisher, B.A., Aufdenkampe, A.K., Yoo, K., Aalto, R.E. and Marquard, J. (2018) Soil carbon redistribution and organo-mineral associations after lateral soil movement and mixing in a first-order forest watershed. *Geoderma*, **319,** 142-155 DOI: https://doi.org/10.1016/j.geoderma.2018.01.006.

Folk, R.L. and Ward, W.C. (1957) Brazos River bar [Texas]; a study in the significance of grain size parameters. *Journal of Sedimentary Research*, **27,** 3-26 DOI: 10.1306/74d70646-2b21-11d7-8648000102c1865d.

Gaillardet, J., Dupré, B., Louvat, P. and Allègre, C.J. (1999) Global silicate weathering and CO2 consumption rates deduced from the chemistry of large rivers. *Chemical Geology*, **159,** 3-30 DOI: https://doi.org/10.1016/S0009-2541(99)00031-5.

Galy, V., France-Lanord, C., Beyssac, O., Faure, P., Kudrass, H. and Palhol, F. (2007) Efficient organic carbon burial in the Bengal fan sustained by the Himalayan erosional system. *Nature*, **450,** 407-410 DOI: 10.1038/nature06273.

Golovneva, L.B. (2010) Variability in epidermal characters of Ginkgo tzagajanica Samylina (Ginkgoales) from the Paleocene of the Tsagayan formation (Amur Region) and the taxonomy of tertiary species of Ginkgo. *Paleontological Journal*, **44,** 584-594 DOI: 10.1134/S003103011005014X.

Grundvåg, S.-A. and Helland-Hansen, W. (2021) The Svalbard Eocene-Oligocene (?) Central Basin succession: Sedimentation patterns and controls: Source to sink and temporal considerations.

Grundvåg, S.-A., Helland-Hansen, W., Johannessen, E.P., Eggenhuisen, J., Pohl, F. and Spychala, Y. (2023) Deep-water sand transfer by hyperpycnal flows, the Eocene of Spitsbergen, Arctic Norway. *Sedimentology*, **70,** 2057-2107 DOI: https://doi.org/10.1111/sed.13105.

Grundvåg, S.-A., Helland-Hansen, W., Johannessen, E.P., Olsen, A.H. and Stene, S.A.K. (2014a) The depositional architecture and facies variability of shelf deltas in the Eocene Battfjellet Formation, Nathorst Land, Spitsbergen. *Sedimentology*, **61,** 2172-2204 DOI: https://doi.org/10.1111/sed.12131.

Grundvåg, S.-A., Johannessen, E.P., Helland-Hansen, W. and Plink-Björklund, P. (2014b) Depositional architecture and evolution of progradationally stacked lobe complexes in the Eocene Central Basin of Spitsbergen. *Sedimentology*, **61,** 535-569 DOI: https://doi.org/10.1111/sed.12067.

Hage, S., Galy, V.V., Cartigny, M.J.B., Acikalin, S., Clare, M.A., Gröcke, D.R., Hilton, R.G., Hunt, J.E., Lintern, D.G., McGhee, C.A., Parsons, D.R., Stacey, C.D., Sumner, E.J. and Talling, P.J. (2020) Efficient preservation of young terrestrial organic carbon in sandy turbidity-current deposits. *Geology*, **48,** 882-887 DOI: 10.1130/g47320.1.

Harland, W.B. and Kay, M. (1969) Contribution of Spitsbergen to Understanding of Tectonic Evolution of North Atlantic Region. In: *North Atlantic—Geology and Continental Drift*, **12**, pp. 0. American Association of Petroleum Geologists.

Hedges, J.I. and Keil, R.G. (1995) Sedimentary organic matter preservation: an assessment and speculative synthesis. *Marine Chemistry*, **49,** 81-115 DOI: https://doi.org/10.1016/0304-4203(95)00008-F.

Helland-Hansen, W. (1990) Sedimentation in Paleogene Foreland Basin, Spitsbergen1. *AAPG Bulletin*, **74,** 260-272 DOI: 10.1306/0c9b22bd-1710-11d7-8645000102c1865d.

Helland-Hansen, W. (1992) Geometry and facies of Tertiary clinothems, Spitsbergen. *Sedimentology*, **39,** 1013-1029 DOI: https://doi.org/10.1111/j.1365-3091.1992.tb01994.x.

Helland-Hansen, W. (2010) Facies and stacking patterns of shelf-deltas within the Palaeogene Battfjellet Formation, Nordenskiöld Land, Svalbard: implications for subsurface reservoir prediction. *Sedimentology*, **57,** 190-208 DOI: https://doi.org/10.1111/j.1365-3091.2009.01102.x.

Helland-Hansen, W. and Grundvåg, S.-A. (2021) The Svalbard Eocene-Oligocene (?) Central Basin succession: Sedimentation patterns and controls. *Basin Research*, **33,** 729-753 DOI: https://doi.org/10.1111/bre.12492.

Johannessen, E. and Steel, R. (2005) Shelf-margin clinoforms and prediction of deepwater sands. *Basin Research*, **17,** 521-550 DOI: 10.1111/j.1365-2117.2005.00278.x.

Johnson, M.R. (1994) Thin section grain size analysis revisited. *Sedimentology*, **41,** 985-999 DOI: https://doi.org/10.1111/j.1365-3091.1994.tb01436.x.

Kao, S.J., Hilton, R.G., Selvaraj, K., Dai, M., Zehetner, F., Huang, J.C., Hsu, S.C., Sparkes, R., Liu, J.T., Lee, T.Y., Yang, J.Y.T., Galy, A., Xu, X. and Hovius, N. (2014) Preservation of terrestrial organic

carbon in marine sediments offshore Taiwan: mountain building and atmospheric carbon dioxide sequestration. *Earth Surf. Dynam.*, **2,** 127-139 DOI: 10.5194/esurf-2-127-2014.

Kellerhals, R., Shaw, J. and Arora, V.K. (1975) On Grain Size from Thin Sections. *The Journal of Geology*, **83,** 79-96, http://www.jstor.org/stable/30062340.

Kellogg, H.E. (1975) Tertiary Stratigraphy and Tectonism in Svalbard and Continental Drift1. *AAPG Bulletin*, **59,** 465-485 DOI: 10.1306/83d91cb3-16c7-11d7-8645000102c1865d.

Kennedy, M.J. and Wagner, T. (2011) Clay mineral continental amplifier for marine carbon sequestration in a greenhouse ocean. *Proceedings of the National Academy of Sciences*, **108,** 9776-9781 DOI: doi:10.1073/pnas.1018670108.

Kneller, B. and Buckee, C. (2000) The structure and fluid mechanics of turbidity currents: a review of some recent studies and their geological implications. *Sedimentology*, **47,** 62-94 DOI: https://doi.org/10.1046/j.1365-3091.2000.047s1062.x.

Krumbein, W.C. (1934) Size frequency distributions of sediments. *Journal of Sedimentary Research*, **4,** 65-77 DOI: 10.1306/d4268eb9-2b26-11d7-8648000102c1865d.

Lasabuda, A., Laberg, J.S., Knutsen, S.-M. and Safronova, P. (2018) Cenozoic tectonostratigraphy and pre-glacial erosion: A mass-balance study of the northwestern Barents Sea margin, Norwegian Arctic. *Journal of Geodynamics*, **119,** 149-166 DOI: https://doi.org/10.1016/j.jog.2018.03.004.

Lee, H., Galy, V., Feng, X., Ponton, C., Galy, A., France-Lanord, C. and Feakins, S.J. (2019) Sustained wood burial in the Bengal Fan over the last 19 My. *Proceedings of the National Academy of Sciences*, **116,** 22518-22525 DOI: doi:10.1073/pnas.1913714116.

Manum, S.B. and Throndsen, T. (1986) Age of Tertiary formations on Spitsbergen. *Polar Research*, **4,** 103-131 DOI: 10.3402/polar.v4i2.6927.

Masson, D.G., Huvenne, V.A.I., de Stigter, H.C., Wolff, G.A., Kiriakoulakis, K., Arzola, R.G. and Blackbird, S. (2010) Efficient burial of carbon in a submarine canyon. *Geology*, **38,** 831-834 DOI: 10.1130/g30895.1.

Mayer, L.M. (1994) Surface area control of organic carbon accumulation in continental shelf sediments. *Geochimica et Cosmochimica Acta*, **58,** 1271-1284 DOI: https://doi.org/10.1016/0016-7037(94)90381-6.

McArthur, A.D., Kneller, B.C., Wakefield, M.I., Souza, P.A. and Kuchle, J. (2016) Palynofacies classification of the depositional elements of confined turbidite systems: Examples from the Gres d'Annot, SE France. *Marine and Petroleum Geology*, **77,** 1254-1273 DOI: https://doi.org/10.1016/j.marpetgeo.2016.08.020.

Milliman, J.D. and Syvitski, J.P.M. (1992) Geomorphic/Tectonic Control of Sediment Discharge to the Ocean: The Importance of Small Mountainous Rivers. *The Journal of Geology*, **100,** 525-544 DOI: 10.1086/629606.

Müller, R.D. and Spielhagen, R.F. (1990) Evolution of the Central Tertiary Basin of Spitsbergen: towards a synthesis of sediment and plate tectonic history. *Palaeogeography, Palaeoclimatology, Palaeoecology*, **80,** 153-172 DOI: https://doi.org/10.1016/0031-0182(90)90127-S.

Myhre, A.M., Eldholm, O. and Sundvor, E. (1982) The margin between Senja and Spitsbergen fracture zones: Implications from plate tectonics. *Tectonophysics*, **89,** 33-50 DOI: https://doi.org/10.1016/0040-1951(82)90033-6.

Paradis, S., Nakajima, K., Van der Voort, T.S., Gies, H., Wildberger, A., Blattmann, T.M., Bröder, L. and Eglinton, T.I. (2023) The Modern Ocean Sediment Archive and Inventory of Carbon (MOSAIC): version 2.0. *Earth Syst. Sci. Data*, **15,** 4105-4125 DOI: 10.5194/essd-15-4105-2023.

Petersen, T., Thomsen, T., Olaussen, S. and Stemmerik, L. (2016) Provenance shifts in an evolving Eurekan foreland basin: the Tertiary Central Basin, Spitsbergen. *Journal of the Geological Society*, **173,** 2015-076 DOI: 10.1144/jgs2015-076.

Petter, A.L. and Steel, R.J. (2006) Hyperpycnal flow variability and slope organization on an Eocene shelf margin, Central Basin, Spitsbergen. *AAPG Bulletin*, **90,** 1451-1472 DOI: 10.1306/04240605144.

Plink-Björklund, P., Mellere, D. and Steel, R.J. (2001) Turbidite Variability and Architecture of Sand-Prone, Deep-Water Slopes: Eocene Clinoforms in the Central Basin, Spitsbergen. *Journal of Sedimentary Research*, **71,** 895-912 DOI: 10.1306/030501710895.

Plink-Björklund, P., Steel, R., Dalrymple, R.W., Leckie, D.A. and Tillman, R.W. (2006) Incised Valleys on an Eocene Coastal Plain and Shelf, Spitsbergen—Part of a Linked Shelf–Slope System. In: *Incised Valleys in Time and Space*, **85**, pp. 0. SEPM Society for Sedimentary Geology.

Plink-Björklund, P. and Steel, R.J. (2004) Initiation of turbidity currents: outcrop evidence for Eocene hyperpycnal flow turbidites. *Sedimentary Geology*, **165,** 29-52 DOI: https://doi.org/10.1016/j.sedgeo.2003.10.013.

Prélat, A., Covault, J.A., Hodgson, D.M., Fildani, A. and Flint, S.S. (2010) Intrinsic controls on the range of volumes, morphologies, and dimensions of submarine lobes. *Sedimentary Geology*, **232,** 66-76 DOI: https://doi.org/10.1016/j.sedgeo.2010.09.010.

Prélat, A., Hodgson, D. and Flint, S. (2009) Evolution, architecture and hierarchy of distributary deep-water deposits: A high-resolution outcrop investigation from the Permian Karoo Basin, South Africa. *Sedimentology*, **56,** 2132-2154 DOI: 10.1111/j.1365-3091.2009.01073.x.

Rabouille, C., Dennielou, B., Baudin, F., Raimonet, M., Droz, L., Khripounoff, A., Martinez, P., Mejanelle, L., Michalopoulos, P., Pastor, L., Pruski, A., Ragueneau, O., Reyss, J.L., Ruffine, L., Schnyder, J., Stetten, E., Taillefert, M., Tourolle, J. and Olu, K. (2019) Carbon and silica megasink in deep-sea sediments of the Congo terminal lobes. *Quaternary Science Reviews*, **222,** 105854 DOI: https://doi.org/10.1016/j.quascirev.2019.07.036.

Saller, A., Lin, R. and Dunham, J. (2006) Leaves in turbidite sands: The main source of oil and gas in the deep-water Kutei Basin, Indonesia. *Aapg Bulletin - AAPG BULL*, **90,** 1585-1608 DOI: 10.1306/04110605127.

Schweitzer, H.-J. (1980) Environment and climate in the early tertiary of spitsbergen. *Palaeogeography, Palaeoclimatology, Palaeoecology*, **30,** 297-311 DOI: https://doi.org/10.1016/0031-0182(80)90062-0.

Sluijs, A. and Dickens, G.R. (2012) Assessing offsets between the δ13C of sedimentary components and the global exogenic carbon pool across early Paleogene carbon cycle perturbations. *Global Biogeochemical Cycles*, **26** DOI: https://doi.org/10.1029/2011GB004224.

Sparkes, R.B., Lin, I.-T., Hovius, N., Galy, A., Liu, J.T., Xu, X. and Yang, R. (2015) Redistribution of multi-phase particulate organic carbon in a marine shelf and canyon system during an exceptional river flood: Effects of Typhoon Morakot on the Gaoping River–Canyon system. *Marine Geology*, **363,** 191-201 DOI: https://doi.org/10.1016/j.margeo.2015.02.013.

Spielhagen, R.F. and Tripati, A. (2009) Evidence from Svalbard for near-freezing temperatures and climate oscillations in the Arctic during the Paleocene and Eocene. *Palaeogeography, Palaeoclimatology, Palaeoecology*, **278,** 48-56 DOI: https://doi.org/10.1016/j.palaeo.2009.04.012.

Spychala, Y.T., Ramaaker, T.A.B., Eggenhuisen, J.T., Grundvåg, S.-A., Pohl, F. and Wróblewska, S. (2021) Proximal to distal grain-size distribution of basin-floor lobes: A study from the Battfjellet Formation, Central Tertiary Basin, Svalbard. *The Depositional Record*, **8,** 436-456 DOI: https://doi.org/10.1002/dep2.167.

Steel, R., Gjelberg, J., Helland-Hansen, W., Kleinspehn, K., Nøttvedt, A. and Rye-Larsen, M. (1985) The Tertiary strike-slip basins and orogenic belt of Spitsbergen. *Strike-slip deformation, basin formation, and sedimentation*, **37,** 339-359 DOI: 10.2110/pec.85.37.0339.

Steel, R. and Olsen, T. (2002) Clinoforms, Clinoform Trajectories and Deepwater Sands, pp. 367-380.

Stetten, E., Baudin, F., Reyss, J.-L., Martinez, P., Charlier, K., Schnyder, J., Rabouille, C., Dennielou, B., Coston-Guarini, J. and Pruski, A.M. (2015) Organic matter characterization and distribution in sediments of the terminal lobes of the Congo deep-sea fan: Evidence for the direct influence of the Congo River. *Marine Geology*, **369,** 182-195 DOI: https://doi.org/10.1016/j.margeo.2015.08.020.

Talling, P.J., Hage, S., Baker, M.L., Bianchi, T.S., Hilton, R.G. and Maier, K.L. (2024) The Global Turbidity Current Pump and Its Implications for Organic Carbon Cycling. *Annual Review of Marine Science*, **16,** 105-133 DOI: 10.1146/annurev-marine-032223-103626.

Talling, P.J., Masson, D.G., Sumner, E.J. and Malgesini, G. (2012) Subaqueous sediment density flows: Depositional processes and deposit types. *Sedimentology*, **59,** 1937-2003 DOI: https://doi.org/10.1111/j.1365-3091.2012.01353.x.

Tyson, R.V. and Follows, B. (2000) Palynofacies prediction of distance from sediment source: a case study from the Upper Cretaceous of the Pyrenees. *Geology*, **28,** 569-571.

Uhl, D., Traiser, C., Griesser, U. and Denk, T. (2007) Fossil leaves as palaeoclimate proxies in the Palaeogene of Spitsbergen (Svalbard). *Acta Palaeobotanica*, **47,** 89-107.

Van der Zwan, C.J. (1990) Palynostratigraphy and palynofacies reconstruction of the Upper Jurassic to Lowermost Cretaceous of the Draugen Field, offshore Mid Norway. *Review of Palaeobotany and Palynology*, **62,** 157-186 DOI: https://doi.org/10.1016/0034-6667(90)90021-A.

van Hinsbergen, D.J.J., de Groot, L.V., van Schaik, S.J., Spakman, W., Bijl, P.K., Sluijs, A., Langereis, C.G. and Brinkhuis, H. (2015) A Paleolatitude Calculator for Paleoclimate Studies (model version 2.1). *PLOS ONE*.

Węglarczyk, S. (2018) Kernel density estimation and its application. *ITM Web Conf.*, **23,** 00037, https://doi.org/10.1051/itmconf/20182300037.

Yedema, Y.W., Sangiorgi, F., Sluijs, A., Sinninghe Damsté, J.S. and Peterse, F. (2023) The dispersal of fluvially discharged and marine, shelf-produced particulate organic matter in the northern Gulf of Mexico. *Biogeosciences*, **20,** 663-686 DOI: 10.5194/bg-20-663-2023.

Zachos, J.C., Dickens, G.R. and Zeebe, R.E. (2008) An early Cenozoic perspective on greenhouse warming and carbon-cycle dynamics. *Nature*, **451,** 279-283 DOI: 10.1038/nature06588.

Supplementary materials

Supplementary figures

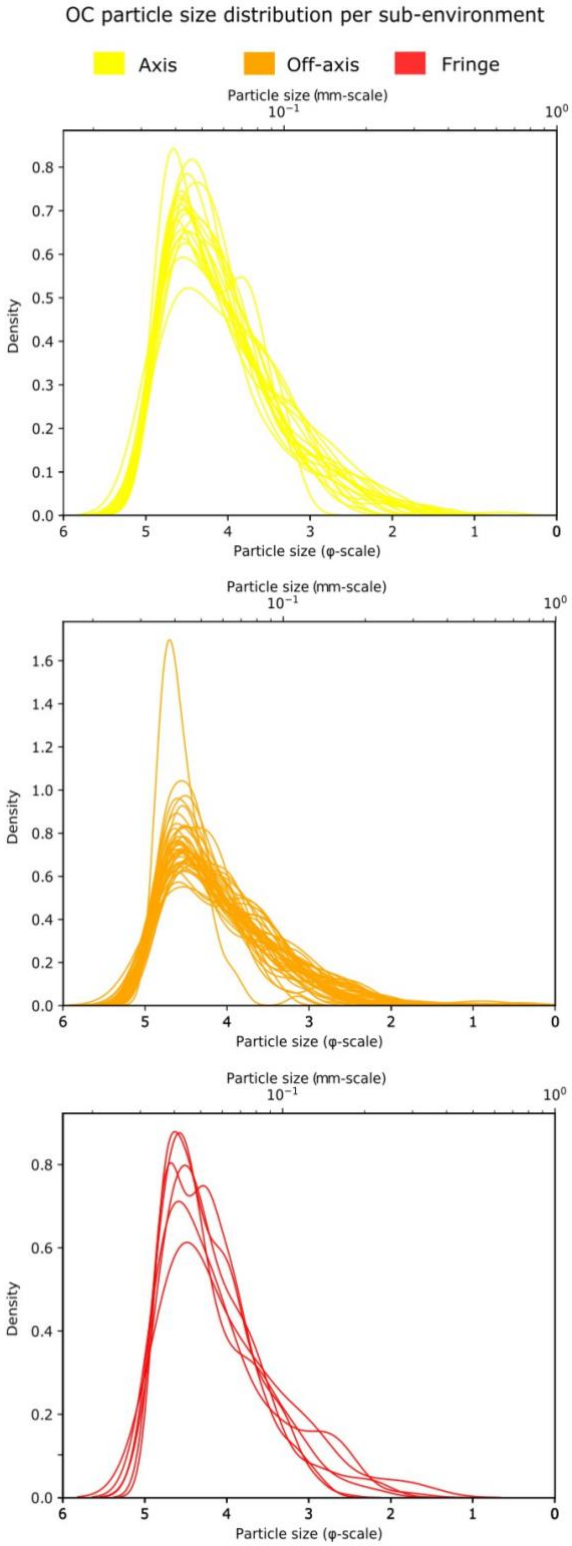

Figure 1: OC particle size density estimations of all particles measured per lobe sub-environment (unweighted). Gray lines are average of all the thin sections of the sub-environment.

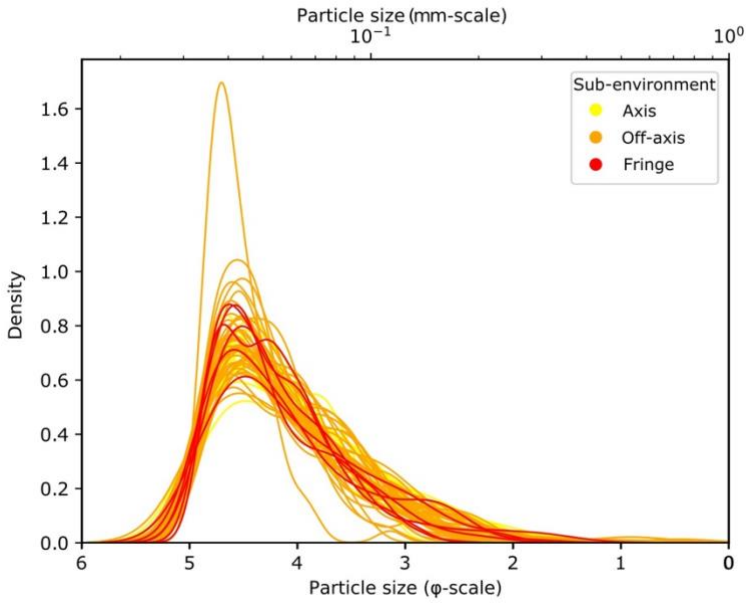

Figure 2: OC particle size density estimation of the lobe axis, off-axis, and fringe sub-environments of Clinothem 12 (unweighted). Gray line indicates the average particle size. Density plot contains all particles analyzed in the thin sections.

Table I: All acquired data

Filename indicates sample (last number) of each of the 8 logs (second number) of Clinoform 12 (CF12).

filename	Distance	Sub-environment	Major axis (µm)	Minor axis (µm)	Mean D (mm)	Mean ϕ	Weighted mean D (mm)	Weighted mean ϕ	Mineral grainsize (Spychala et al., 2021)	OC area % (not used)	TOC (wt%)	δ13C (‰VPDB)
CF12_02_01.csv	0	offaxis	81.2998095	36.8368214	0.06036216	4.12487284	0.09850204	3.45293207	0.144	0.00961665	0.16	
CF12_02_02.csv	0	offaxis	101.23521	36.74575	0.05762662	4.21510803	0.64790741	0.79035087	0.1453	0.02925763	0.43	
CF12_02_03.csv	0	offaxis	83.6055943	36.223217	0.05743911	4.2035813	0.16258758	2.84102944	0.1523	0.01381111	0.15	-20.56
CF12_02_04.csv	0	offaxis	91.0070083	39.4066033	0.0627424	4.11442449	0.16338571	2.76936022	0.1798	0.01957884	0.69	
CF12_02_05.csv	0	offaxis	76.9650652	31.7903044	0.05122556	4.33882911	0.12255512	3.21889472	0.1397	0.00913506	0.25	
CF12_02_06.csv	0	offaxis	92.5985169	41.9107191	0.06529697	4.03473259	0.13319542	3.01821336	0.2337	0.01440552	0.23	
CF12_02_07.csv	0	axis	96.1157042	41.809833	0.06384975	4.08811354	0.104971	3.37998021	0.1865	0.12153204	0.15	
CF12_02_08.csv	0	axis	92.0828887	42.1248544	0.0620074	4.11422345	0.21896959	2.40110991	0.2137	0.09098063	0.21	
CF12_02_09.csv	0	axis	95.033042	41.7575796	0.0637143	4.0835272	0.11390964	3.32987639	0.1649	0.12895972	0.27	
CF12_02_10.csv	0	axis	89.4503815	41.5016156	0.0632136	4.09913296	0.16704305	2.74403778	0.1568	0.05812275	0.14	-20.66
CF12_02_11.csv	0	axis	80.9972925	34.5200849	0.05496163	4.254839	0.10964411	3.30535179	0.1578	0.0121557	0.17	-19.26
CF12_02_12.csv	0	offaxis	85.8328634	34.1243416	0.05717513	4.19916772	0.09543922	3.55292794	0.1125	0.01825288	0.19	
CF12_03_01.csv	150	offaxis	93.5959451	43.1237582	0.06666456	4.0502882	0.21747794	2.42367052	0.1811	0.01725074	0.14	
CF12_03_02.csv	150	offaxis	76.4970332	34.2961706	0.05436548	4.25851998	0.10016217	3.42770798	0.0896	0.02156739	0.52	
CF12_03_03.csv	150	offaxis	93.5222828	39.0818621	0.06245052	4.10589228	0.13024653	3.11811113	0.1526	0.0236137	0.23	-20.08
CF12_03_04.csv	150	offaxis	77.6533009	40.6352478	0.06073051	4.1347461	0.16684832	2.76163933	0.1422	0.01413243	0.27	
CF12_03_05.csv	150	axis	92.3072079	39.9625941	0.06553064	4.03970431	0.4480617	1.41833496	0.1807	0.01599624	0.26	
CF12_03_06.csv	150	axis	95.4735738	37.526082	0.06113067	4.14318391	0.09770454	3.4543181	0.173	0.01064815	0.14	
CF12_03_07.csv	150	axis	101.323944	45.1299111	0.0699661	3.98167374	0.15137398	2.89366639	0.187	0.01892677	0.17	
CF12_03_08.csv	150	axis	84.6285581	40.5456047	0.06280679	4.10509457	0.23161711	2.35995295	0.1496	0.01270417	0.35	-22.96
CF12_03_09.csv	150	axis	91.3123284	39.5450672	0.06553702	4.05777903	0.0651976	3.99876511	0.1562	0.02014834	0.14	
CF12_03_10.csv	150	offaxis	76.6103951	30.393142	0.05160162	4.32428368	0.05997889	4.1802676	0.1063	0.0142636	0.61	-24.15
CF12_04_01.csv	445	offaxis	91.5161881	39.2132376	0.05965902	4.16005574	0.08758719	3.62847944	0.1629	0.01717523	0.2	
CF12_04_02.csv	445	offaxis	80.3862821	35.435609	0.05788273	4.18394905	0.10191644	3.44142972	0.134	0.01706091	0.19	
CF12_04_03.csv	445	axis	90.593188	39.6791026	0.06342567	4.10332388	0.11443435	3.24338984	0.1548	0.01891132	0.3	
CF12_04_04.csv	445	axis	83.6052243	38.5411122	0.05799282	4.17379286	0.16835085	2.73386793	0.1418	0.01576938	0.29	
CF12_04_05.csv	445	axis	88.6628539	40.9365308	0.06043565	4.11984006	0.09507002	3.50007084	0.1602	0.02062025	0.14	-19.87
CF12_04_06.csv	445	offaxis	84.4527531	35.4555803	0.05812514	4.19220245	0.12088777	3.18120091	0.1695	0.00997528	0.14	
CF12_05_09.csv	1352	offaxis	93.7950476	43.5384714	0.06747702	4.00832131	0.10284917	3.38807898	0.1327	0.03718271	0.4	-22.42
CF12_05_10.csv	1352	offaxis	106.742512	38.7978146	0.06418019	4.08594149	0.46583834	1.27038206	0.124	0.05049133	0.96	
CF12_05_11.csv	1352	offaxis	84.7941654	34.2285669	0.05759459	4.19988657	0.14027432	3.02571517	0.0939	0.01425877	0.32	-22.91
CF12_05_12.csv	1352	offaxis	93.3767972	37.0134406	0.06405472	4.08058605	0.06972356	3.91943809	0.131	0.02141442	0.35	
CF12_05_13.csv	1352	offaxis	91.738985	43.3488647	0.06624251	4.0566371	0.11288333	3.2896659	0.132	0.02522661	0.16	
CF12_05_14.csv	1352	axis	83.1465512	36.7987717	0.05798221	4.17910349	0.08498235	3.65915568	0.1467	0.01602249	0.27	-22.33
CF12_05_15.csv	1352	axis	90.7447822	39.451099	0.06091193	4.14022391	0.13970658	2.96969188	0.1493	0.01664307	0.19	-20.44
CF12_05_16.csv	1352	axis	75.2760351	34.4521579	0.05500466	4.24717672	0.09776839	3.45465699	0.1348	0.00533938	0.3	
CF12_05_17.csv	1352	axis	76.9414725	33.7217528	0.05383393	4.27957498	0.13680877	3.01341416	0.1241	0.01833073	0.4	
CF12_05_18.csv	1352	offaxis	64.2725875	31.5481375	0.05025328	4.35783326	0.1463937	2.90825085	0.1136	0.00577043	0.28	
CF12_05_19.csv	1352	offaxis	51.96764	29.4344267	0.04270044	4.56455782	0.13824908	3.0414282	0.026	0.00398219	0.45	
CF12_05_20.csv	1352	offaxis	71.9688514	34.9552973	0.05407402	4.26633504	0.17256707	2.69387924	0.1339	0.01388831	1.12	-25.06
CF12_06_01.csv	2289	offaxis	71.9044237	33.697339	0.0504294	4.34221561	0.42791084	1.54248825	0.1288	0.00554388	0.18	
CF12_06_02.csv	2289	offaxis	80.8213798	36.2812152	0.05924253	4.1947948	0.25832475	2.17911847	0.1316	0.00955937	0.22	-20.91
CF12_06_03.csv	2289	offaxis	81.8395294	44.7167794	0.06120333	4.13744444	0.22136984	2.3687507	0.1265	0.01114624	0.22	
CF12_06_04.csv	2289	axis	80.5063881	35.9218582	0.05674641	4.2000246	0.16341853	2.75105258	0.1514	0.01462873	0.33	
CF12_06_05.csv	2289	axis	78.0899552	38.323209	0.05718529	4.18635519	0.12261805	3.17843924	0.1449	0.00778809	0.32	
CF12_06_06.csv	2289	offaxis	74.9783854	35.4086771	0.05644407	4.23736977	0.15757306	2.84406078	0.1486	0.00983798	0.18	-21.21
CF12_07_05.csv	2932	offaxis	89.0697312	37.8282258	0.0616963	4.11043739	0.19993141	2.49753296	0.1571	0.01260938	0.24	
CF12_07_06.csv	2932	offaxis	88.7803585	36.5013679	0.06096931	4.10963555	0.17867821	2.62009988	0.1153	0.01315815	0.29	
CF12_07_07.csv	2932	offaxis	102.702885	42.6730192	0.06563457	4.07144823	0.1629764	2.81907259	0.1196	0.01486651	0.36	
CF12_07_08.csv	2932	offaxis	82.063084	36.6569237	0.05737333	4.20310962	0.12804441	3.07486424	0.1312	0.01647829	0.17	
CF12_07_09.csv	2932	offaxis	66.5303535	32.2476379	0.05030062	4.3540488	0.16206683	2.78436674	0.1312	0.00884482	0.31	
CF12_07_10.csv	2932	offaxis	84.4996182	37.0282818	0.05900139	4.1598407	0.25663636	2.27419795	0.1084	0.01348724	0.25	-20.92

CF12_07_11.csv	2932	offaxis	72.9107375	34.1200618	0.05387784	4.26959257	0.15712651	2.82079037	0.0849	0.02388708	0.2	-22.78
CF12_08_07.csv	3632	fringe	100.081429	40.9645714	0.06454725	4.09069627	0.13773667	3.04237885	0.1526	0.01427816	0.41	
CF12_08_08.csv	3632	fringe	83.3024733	36.345542	0.05621279	4.22214906	0.1989008	2.54702565	0.1022	0.01685154	0.22	
CF12_08_09.csv	3632	offaxis	85.7285565	38.0534677	0.05708928	4.21394112	0.07669534	3.76191748	0.1341	0.01755778	0.18	
CF12_08_10.csv	3632	offaxis	78.318876	36.0483141	0.0565683	4.2185799	0.09740064	3.47652509	0.1442	0.01316573	0.15	
CF12_08_11.csv	3632	offaxis	81.6914286	37.1543247	0.05525122	4.2478532	0.10026548	3.44094546	0.1653	0.00997722	0.15	-20.2
CF12_08_12.csv	3632	offaxis	92.7371899	38.232481	0.06272369	4.09244444	0.10523596	3.36650844	0.1513	0.01207209	0.3	-23.4
CF12_08_13.csv	3632	offaxis	79.8830837	36.4902118	0.05553734	4.24967315	0.22715782	2.31665227	0.1151	0.02475986		
CF12_08_14.csv	3632	offaxis	94.7527399	42.6746705	0.06698627	4.02356535	0.14852417	2.93564939	0.1517	0.03151919	0.17	
CF12_HS_04.csv	4715	fringe	73.5761084	35.0763775	0.05492554	4.25198914	0.08766204	3.61277282	0.0598	0.04813932	0.38	-23.58
CF12_HS_05.csv	4715	fringe	72.4067639	34.8370694	0.05348115	4.27658212	0.0848454	3.65562823	0.0901	0.02018469	0.3	
CF12_HS_06.csv	4715	fringe	0	0	0	0	0.16362111	2.77506832	0.0831	0	0.44	-23.89
CF12_HS_07.csv	4715	fringe	91.0684702	38.3437947	0.06255642	4.11814216	0.12846346	3.13231394	0.137	0.02374674	0.38	
CF12_HS_08.csv	4715	fringe	81.998127	34.8130952	0.05655207	4.22650845			0.1256	0.02224608	0.39	